Li *et al. Energy Mater* 2024;4:400046
DOI: 10.20517/energymater.2023.147

Energy Materials

Review

Open Access

Check for updates

Electrochemically nitrate remediation by single-atom catalysts: advances, mechanisms, and prospects

Zhe Li[1], Chuanju Yang[2], Bin Xu[1], Li Yao[2], Wenlei Zhu[2,*], Yibin Cui[1,*]

[1]Nanjing Institute of Environmental Sciences, Ministry of Ecology and Environment of the People's Republic of China, Nanjing 210042, Jiangsu, China.
[2]State Key Laboratory of Pollution Control and Resource Reuse, State Key Laboratory of Analytical Chemistry for Life Science, the Frontiers Science Center for Critical Earth Material Cycling, School of the Environment, School of Chemistry and Chemical Engineering, Nanjing University, Nanjing 210023, Jiangsu, China.

***Correspondence to:** Prof. Wenlei Zhu, State Key Laboratory of Pollution Control and Resource Reuse, State Key Laboratory of Analytical Chemistry for Life Science, the Frontiers Science Center for Critical Earth Material Cycling, School of the Environment, School of Chemistry and Chemical Engineering, Nanjing University, 163 Xianlin Road, Qixia District, Nanjing 210023, Jiangsu, China. E-mail: wenleizhu@nju.edu.cn; Prof. Yibin Cui, Nanjing Institute of Environmental Sciences, Ministry of Ecology and Environment of the People's Republic of China, 8 Jiangwangmiao Street, Nanjing 210042, Jiangsu, China. E-mail: cyb@nies.org

How to cite this article: Li Z, Yang C, Xu B, Yao L, Zhu W, Cui Y. Electrochemically nitrate remediation by single-atom catalysts: advances, mechanisms, and prospects. *Energy Mater* 2024;4:400046. https://dx.doi.org/10.20517/energymater.2023.147

Received: 31 Dec 2023 **First Decision:** 20 Mar 2024 **Revised:** 16 Apr 2024 **Accepted:** 9 May 2024 **Published:** 16 May 2024

Academic Editors: Porun Liu, Hao Liu **Copy Editor:** Fangyuan Liu **Production Editor:** Fangyuan Liu

Abstract

Electrocatalytic nitrate reduction reaction (NITRR) is highly desirable for remediating nitrate (NO_3^-) pollution and producing ammonia (NH_3) under mild conditions. To date, great efforts have been made to fabricate selective, efficient, and stable electrocatalysts for NITRR. Among the numerous strategies, single-atom catalysts (SACs) have received extensive interest and investigations due to their cost-effective and maximum atomic utilization. However, the further development of SACs-based NITRR remains hindered by a poor understanding of their in-depth mechanisms. Consequently, this review summarizes the recent advances of SACs for the NITRR, including Cu-SACs, Fe-SACs, Zn-SACs, Co-SACs, and single-atom alloys. In addition, the characterization techniques for SACs and reaction pathways of NITRR are presented to give a robust understanding of SACs-based NITRR. Finally, we analyze the current challenges in fabricating SACs for NITRR, while the key factors for further improving NITRR performances are also examined.

Keywords: Single-atom catalysts, electrocatalytic nitrate reduction reaction, electronic structure, characterization techniques

© The Author(s) 2024. **Open Access** This article is licensed under a Creative Commons Attribution 4.0 International License (https://creativecommons.org/licenses/by/4.0/), which permits unrestricted use, sharing, adaptation, distribution and reproduction in any medium or format, for any purpose, even commercially, as long as you give appropriate credit to the original author(s) and the source, provide a link to the Creative Commons license, and indicate if changes were made.

INTRODUCTION

Nitrogen (N) is significant to the agricultural production[1]. The synthesis and employment of nitrogenous fertilizers have made outstanding contributions to increasing agro-food production and ensuring that human society is no longer suffering from food shortage[2,3]. As the world population grows, the excessive use of nitrogenous fertilizers, fossil fuel combustion, and industrial activities lead to a dramatic increase in discharging nitrate (NO_3^-) to water sources[4]. The release of nitrate-containing wastewater will breach the balance of the nitrogen cycle and bring a range of ecological issues such as eutrophication and drinking water contamination[5,6]. Since the quality of drinking water relates directly to human health, the remediation of nitrate-containing wastewater is becoming a longstanding and challenging task in the current situation. Theoretically, heterotrophic denitrifying bacteria can completely transform NO_3^- to the harmless nitrogen gas (N_2)[7]. However, the denitrifying system requires a long resident time, restricting its large-scale application. Meanwhile, employing carbon sources will cause secondary pollution to the waterbody[8,9]. Additionally, a highly concentrated NO_3^- wastewater is also prejudicial to the growth of denitrifying bacteria and not conducive to the denitrifying system[10]. Hence, developing efficient and sustainable methods for nitrate-contaminated water source purification is of great significance to both ecological and environmental governance.

In addition to converting nitrates to N_2, ammonia (NH_3) synthesis offers a promising approach to mitigate the pollution of NO_3^- and realize nitrogen recovery[11]. In recent years, electrocatalytic nitrate reduction reaction (NITRR) methods have been considered promising for converting nitrate to ammonia[12-18]. The nine protons and eight electrons transfer process ($NO_3^- + 9H^+ + 8e^- \rightarrow NH_3 + 3H_2O$) contributes to an efficient and controllable process to produce NH_3 under mild conditions, avoiding the huge energy consumption in the Haber-Bosch (H-B) process[15]. Particularly, the high solubility makes NO_3^- have great compatibility with the liquid-based electrocatalytic systems and alleviates the reaction energy barrier[16]. On the other hand, the protons in the electrocatalytic process directly originate from water dissociation, which can reduce the CO_2 emissions of the industrial H_2 production. Using NO_3^- as the N-feedstock, the relatively weak bond of N=O (204 kJ mol^{-1}) makes NITRR have more positive operating potential than N_2 (N≡N bond, 941 kJ mol^{-1})[15-18]. With the development of renewable energy sources, electric-driven catalytic reactions will have a broader prospect in producing NH_3 and other chemical compounds, which positions the NITRR method as a promising alternative to the conventional H-B process in future applications. Therefore, it is crucial to exploit optimal electrocatalytic systems to meet the practical demands of NO_3^- elimination and NH_3 synthesis.

Single-atom materials are defined as uniformly exposed metal atom sites on the surface of conductive supports such as metal-organic frameworks (MOFs), zeolites, porous carbons, *etc.*[19-21]. By achieving nearly 100% atom utilization efficiency, Single-atom catalysts (SACs) lower the cost in synthesizing effective catalysts and provide model systems to bridge the gap between heterogeneous and homogeneous catalysts[22-25]. Due to their unique electronic properties, SACs have demonstrated the superior activities and capabilities in facilitating the electrocatalytic activities by rational structural design with numerous applications of NITRR[26], hydrogen evolution (HER)[27,28], oxygen evolution (OER)[29,30], oxygen reduction (ORR)[31-34], carbon dioxide reduction (CO_2RR)[35-38], nitrogen reduction (NRR)[39], and carbon-nitrogen coupling reactions (C-N coupling)[40]. Since transition metals (TMs) have excellent electronic properties to adsorb and reduce nitrate due to the unique d-orbital electron arrangement, they were employed to fabricate SACs for NITRR in recent studies. Theoretically, SACs are more favorable in producing ammonia since the isolated single atoms cannot form N-N bonds during the NITRR process[41]. To prevent the aggregation of single-atom active sites, the metal loading of SACs is hard to exceed 1 at.% in most strategies. Therefore, the effective site number on SACs is far less than on other catalysts[42]. It can be anticipated that

SACs are unsuitable for large-scale ammonia production, but they can still serve as an effective catalyst for nitrogen recovery from nitrate-polluted wastewater. Nevertheless, the specific pathways and mechanisms of SACs for NITRR processes remain poorly understood, highlighting the need for systematic exploration. A comprehensive discussion of SACs for NITRR applications would deepen our understanding of corresponding mechanisms and provide new insights for SAC design.

To this end, the review summarizes the advances of SACs for NITRR applications. By categorizing SACs as Cu, Fe, other SACs (zinc (Zn)-, cobalt (Co)-, zirconium (Zr)-, and nickel (Ni)-SACs), and single-atom alloys (SAAs), it explores the relationship between characteristic active sites and properties and the techniques for SAC characterization. By recognizing the unique structures and properties of SACs in NITRR, the mechanisms, advantages, and challenges are fully discussed. It is worth noting that research of SACs for NITRR is still in its early stages. Therefore, by summarizing the recent advances of NITRR-based SACs, we hope this review can refine the routes for electrocatalytic NO_3^- to NH_3 reduction and shed light on the further development of nitrate remediation.

SACS FOR NITRR

Cu SACs

Cu has unpaired d-electrons and similar d-band energy to the LUMO (lowest unoccupied molecular orbital) Π anti-bonding orbital of NO_3^-[43]. The tunable electronic structure, high abundance, flexible electrochemical activity, low cost, and good electron injection properties make Cu-based catalysts an optimal candidate for NITRR[44]. Although Cu-based catalysts demonstrated relatively high NITRR activities, their large overpotential, nitrite accumulation, and poor catalyst stability still limit their further applications. As mentioned, SACs have nearly 100% atom utilization efficiency, and Cu SACs can be desirable candidates to improve the NITRR performance[22]. Therefore, tremendous investigations have emerged to develop selective, efficient, and robust Cu SACs with lower operating potentials in the past five years.

Zhao *et al.* proposed a Cu SAC with boron-doped carbon nitride (BCN) heterojunction for treating nitrate to ammonia[45]. By exchanging counter anion NO_3^- to large-sized *closo*-$[B_{12}H_{12}]^{2-}$, the 1,10-phenanthroline-Cu^{2+} complex exhibits a uniform diamond-shaped nanosheet structure with Cu-N_4 sites. As a result, the BCN@Cu performs 83.95 mg h^{-1} mg_{cat}^{-1} NH_3 yield rate, 97.37% Faradaic efficiency at -0.6 V *vs.* Reversible Hydrogen Electrode (RHE). Their follow-up study found that the 1,10-phenanthroline-Cu^{2+}-*closo*-$[B_{12}H_{12}]^{2-}$ structure has the chance to strengthen the attachment to carbon nanotube (CNT) carriers and form BCN@Cu/CNT after pyrolysis[46]. On the other hand, the doping of boron (B) facilitates the formation of the local electric field, enveloping the reaction in a huge electric field atmosphere. As a result, the electronic property and physicochemical stability of the catalyst are greatly improved, and considerable BCN@Cu/CNT conductivity is achieved. With a high NH_3 yield of 172.2265 mg h^{-1} mg_{cat}^{-1} and 95.32% Faradaic efficiency at -0.6 V *vs.* RHE, BCN@Cu/CNT exhibits three times NITRR activity than that of BCN@Cu [Figure 1A and B]. Meanwhile, it presents high performance in purifying nitrate solution with low concentrations. In low-concentration nitrate solutions, BCN@Cu/CNT prefers to convert nitrate to N_2 without the accumulation of NO_2^-, making it an effective catalyst to treat nitrate-containing wastewaters in different application scenarios.

Porous-rich MOFs are great candidates for anchoring single atoms due to their well-defined channel structure and structural diversity. In this class of materials, zeolitic imidazolate frameworks (ZIFs) are the most commonly used substrates owing to their facile synthesis, high surface area, and high porosity. Zhu *et al.* synthesized Cu-N-C catalysts by the pyrolysis of Cu-MOF, which were labeled as Cu-N-C-T

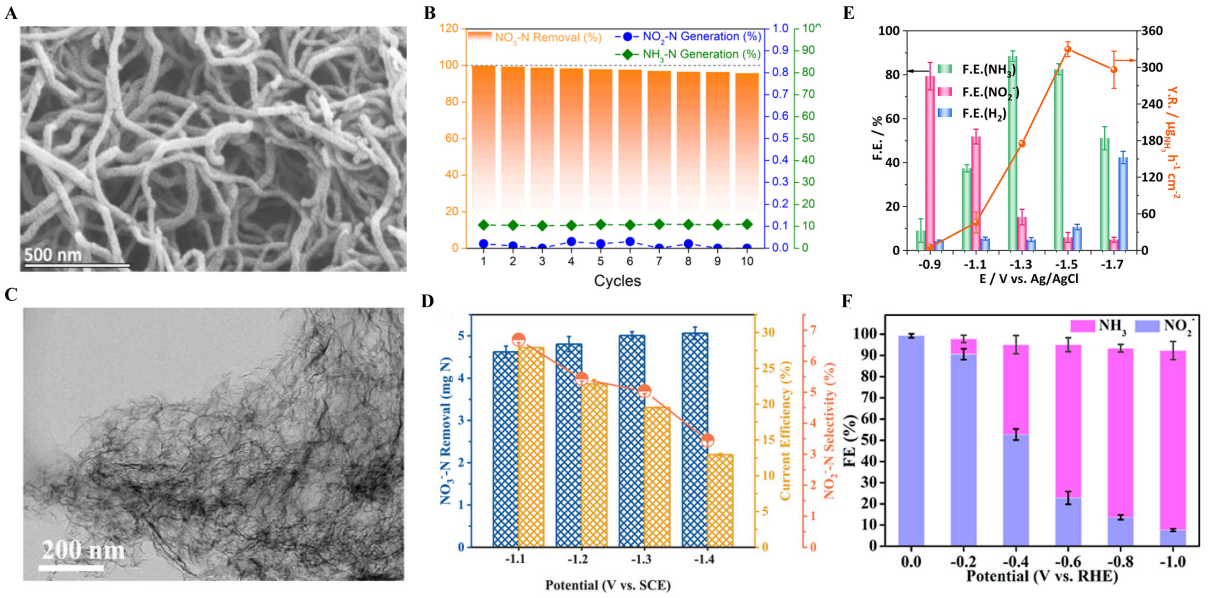

Figure 1. (A) Structure investigation of BCN@Cu/CNT by SEM characterization; (B) NO_3^- removal efficiency of BCN@Cu/CNT. This figure is quoted with permission from Zhao *et al.*[46]; (C) TEM image of Cu-N-C-800; (D) The removal of NO_3^- and current efficiency using Cu-N-C-800. This figure is quoted with permission from Zhu *et al.*[47]; (E) Product distribution of NITRR process using Cu SAAs as the electrocatalyst at varying potentials. This figure is quoted with permission from Li *et al.*[52]; (F) FEs of NH_3 and NO_2^- using Cu-N-C-SAC at different applied potentials. This figure is quoted with permission from Yang *et al.*[53].

according to the temperature of pyrolysis[47]. They found that increasing pyrolysis temperature leads to an aggregation of Cu atoms and nanoparticle/cluster formation on the nanosheets. In Cu-N-C-800, Cu-N_2 and Cu-N_4 active sites were characterized, allowing this unique catalyst to achieve the best catalytic performance in NITRR. The NO_3^- conversion rate can reach 97.3% with a 46.7% current efficiency at -1.3 V *vs.* Saturated Calomel Electrode (SCE, Figure 1C and D). From theoretical calculations, NO_3^- and NO_2^- are more easily adsorbed on carbon nanosheets stabilized Cu-Nx sites than Cu nanoparticles (CuNPs) and bulk Cu, promoting the yield rates of NH_3 production. Chen *et al.* synthesized a Cu-N-C catalyst with Cu-N_4 active sites by the ion exchange of ZIF-8, followed by a coordinative pyrolysis process[41]. The as-prepared Cu-N-C catalyst shows a 100% NO_3^- conversion rate, 94% ammonia selectivity, and 0.25 mg h^{-1} mg_{cat}^{-1} at -1.5 V *vs.* SCE. Due to the strong affinity of Cu-N_4 sites, barely any nitrite was released into the solution after the treatment. Since N-N coupling is thermodynamically unfavored to occur on the single sites of SACs, the reduced N-intermediates are inclined to generate NH_3 rather than N_2, N_2O, or NH_2NH_2. Zhao *et al.* adopted a similar approach to synthesizing Cu SACs by carbonizing the Cu-doped ZIF-8[48]. Unlike the Cu-N-C catalyst, the N-doped porous carbon-anchored single-atom Cu catalyst (Cu_{SA}NPC) suffered a structural collapse after pyrolysis rather than maintaining the morphology of ZIF-8. However, it still performed 87.2% NH_3 Faradaic efficiency (FE_{NH3}) with an NH_3 yield rate of 5.204 mg h^{-1} mg_{cat}^{-1} at -1.4 V *vs.* RHE.

According to density functional theory (DFT) calculations, the performance of most planer substrate-supported Cu-N_4 is unsatisfactory. To this end, Xue *et al.* reported a Cu site anchored micro-mesoporous N-doped carbon (Cu MNC)[49]. Cu MNC-7 demonstrated a considerable NITRR process with 94.8% NO_3^- conversion, 92.922 mg h^{-1} mg_{cat}^{-1} NH_3 yield rate at -0.64 V *vs.* RHE by changing urea/Cu^{2+} molar ratio to 7. Compared to Cu-N-C, the specific surface area and pore structure are increased in the skeleton of Cu MNC-7. In Cu MNC-7, the Cu atom formed three single bonds to connect with nitrogen and one bond to connect with carbon, giving Cu-N_3-C sites more specific electronic and geometric configurations than

Cu-N_4 sites. Wang *et al.* designed a low-coordinated Cu-N_3 SAC and constructed it on a high-curvature hierarchically porous N-doped CNT (NCNT) to get Cu-N_3 SACs/NCNT[50]. By achieving a 1D hollow tubular structure with an inner diameter of ≈ 30 nm and a wall thickness of ≈ 15 nm, Cu-N_3 SACs/NCNT exhibits a 98% NO_3^- conversion, 89.64% FE_{NH3} and 30.09 mg h^{-1} mg_{cat}^{-1}at -0.8 V *vs.* RHE in NITRR. Based on the DFT calculations, they found the NO*, HNO*, H_2NO*, H_2NOH*, and NH_2* pathways are consistent with differential electrochemical mass spectrometry (DEMS) results. Moreover, the intermediates on Cu-N_3 exhibit a lower Gibbs free energy than that of Cu-N_4, which suggests the NITRR process has better reaction dynamics on the 3N coordination structure than the 4N coordination structure. Furthermore, their results demonstrate that low-coordinated CuN_3 sites greatly influence the spin state of Cu, which can promote the NITRR process with the existence of high-curvature carbon. Focusing on the raises of d-orbital energy of Cu-N_4 sites, Wang *et al.* proposed a phosphorus (P)-modified Cu-N_4 SAC (Cu-N_4/P) to minimize the d-orbital energy level caused by unfavorable intermediate adsorption on Cu-N_4[51]. Introducing less electronegative element P promotes the electron transfer from active sites to intermediates. As a result, Cu-N_4/P exhibits a 100% NO_3^- conversion, 95.89% FE_{NH3}, and 2.01 mg h^{-1} mg_{cat}^{-1}at -0.6 V *vs.* RHE in NITRR. DFT calculation results indicated that the formation of NOH* becomes easier on Cu-N_4/P, which can boost the NITRR process in neutral mediums.

Li *et al.* reported a functional single-atom aerogel (Cu-SAA) containing 3D channel framework structure with coordinated Cu single-atom sites[52]. In addition to having an 87% FE_{NH3} and > 0.3 mg cm^{-2} h^{-1} NH_3 yield rate in NITRR, the aerogel also exhibited a remarkable performance for detecting NO_3^- and NH_4^+ [Figure 1E]. Further implementing Cu-SAA in a smart and sustainable fertilizing system (SSFS) enables simultaneous ammonia production and monitoring of NO_3^- and NH_4^+ concentrations during reaction. In addition, the proposed system realized high feasibility for controlling the real-time concentrations of NO_3^-/NH_4^+ in the simulated water streams. Although the presented method did not obtain excellent performance in improving the NH_3 yield rate, the results demonstrated the potential of SAC-supported NITRR in sustainable smart farming approaches.

Although SACs exhibited great potential in transforming NO_3^- to NH_3, it remains controversial for the key factors and mechanisms in SACs-driven NITRR. To this end, Yang *et al.* employed Cu-N-C SAC as the model catalyst to investigate the evolution of Cu active sites by operando X-ray absorption spectroscopy (XAS) at the Cu K-edge during the NITRR process[53]. By operating potentials from 0.00 to -1.00 V *vs.* RHE, a successive morphological transformation of Cu could be observed in the following order: Cu-N_4 → Cu-N_3 → Cu^0 single atoms → Cu^0 aggregates. According to the results of X-ray absorption near edge spectroscopy (XANES) spectra, the edge energy of Cu K-edge spectra continuously decreases with changing potentials due to the reduction of Cu species. When the reduction potential was applied to the Cu-N-C catalyst, Cu^{2+} priorly disappeared in the Cu structure, while Cu^+ maintained the catalyst structure with a declined Cu^+/Cu^0 ratio. Interestingly, minor contributions were achieved from the N-doped carbon embedded Cu^+ (48.3%), while the remaining 50% Cu tended to create a dynamic equilibrium between Cu^0 and Cu^+ and dominated the Faradaic efficiency of NITRR. Compared to $NaBH_4$-reduced CuNPs/N-C, the *in-situ* formed Cu^0 aggregates are more favorable to the NITRR process due to the higher selectivity to NO_2^- on CuNPs/N-C [Figure 1F]. However, this work only investigated the evolution of one Cu-N-C catalyst in NITRR. The universality of their theory still needs to be verified. In the subsequent SAC-driven NITRR studies, accurately defining the actual active sites is urgent rather than arbitrarily attributing the activity to the metal-N sites.

Fe SACs

Since iron is earth-abundant and has moderate adsorption ability to oxygen and nitrogen, numerous studies have emerged to treat nitrogen based on the Fe-containing materials (Fe-based H-B catalysts, nitrogenase

enzymes, *etc.*)[54]. Zero-valent iron was first used for nitrate removal to produce harmless N_2 in water resources, and its particle size directly influenced the nitrogen removal efficiency[55]. However, metallic Fe tends to form iron oxides with poor conductivity and activity which can lead to the passivation, leaching, and dissolution effects on the surface of Fe catalysts. In this case, Fe SACs were designed to minimize the disadvantages with boosted surface area and a significantly improved performance for NITRR.

Wu *et al.* developed Fe SACs with Fe-N_4 active sites for NITRR[56]. The lower thermodynamic barrier of Fe-N_4 active sites greatly contributes to the NITRR efficiency accompanied by the optimal choice of electrolytes, NO_3^- concentration, and the operating voltage. With suppressive HER and N-N coupling process, a significantly improved NH_3 yield rate (~0.46 mmol h^{-1} cm^{-2}) can be achieved with a maximal FE_{NH3} of ~75% by Fe SACs at -0.66 V *vs.* RHE. To simplify the large-scale catalyst production, Song *et al.* proposed a facile one-step hydrothermal method to fabricate the Fe SACs for NITRR[57]. Using graphitic carbon nitride (g-C_3N_4) as the low-cost substrate, the asymmetric charge distribution on g-C_3N_4 can facilitate the stabilization of Fe atoms and affect the performance of Fe SACs [Figure 2A-D]. As a result, the Fe-gC_3N_4 realized a nitrogen-removal capacity of 9,857.5 mg N/g Fe with a high Faradaic efficiency of 77.3%. According to the X-ray absorption fine structure (XAFS) results and the Fourier-transformed extended XAFS (FT-EXAFS) of Fe-gC_3N_4, the Fe atom is more inclined to coordinate with N sites to form Fe-N_4 rather than coordinate with other Fe atoms. On the other hand, the conversion of NH_3 or NO_2^- is inhibited and produces harmless N_2 with the participation of Cl^- in the electrolytes. However, it can be observed that the addition of NaCl slightly declines the NO_3^- to NH_3 efficiency, which can be ascribed to the Cl^- occupied active sites and the overoxidation of NH_3. By adjusting the symmetry of electronic density, the asymmetric coordination structure on MOFs-derived SACs improved the intrinsic activity of SACs. However, the fabrication of MOFs-derived SACs always underwent complicated steps. To this end, Zhang *et al.* designed an optimal way to fabricate a FeN_2O_4 structure through self-assembly [Figure 2E][58]. After one-step pyrolysis, Fe SAC with FeN_2O_2 configuration was obtained and exhibited 92% FE_{NH3} with an NH_3 yield rate of 46 mg h^{-1} mg_{cat}^{-1} [Figure 2F]. Based on the theoretical calculations, NO_3^- is more easily to adsorb on the FeN_2O_2 and forms NO_3* than on FeN_4, which could be attributed to the closer d-band center of FeN_2O_2 to the fermi level and increased density of states (DOS) of the FeN_2O_2 configuration [Figure 2G and H]. Moreover, the inhibition of NO_2^- formation was ascribed to the high energy barrier of NO_3^- to NO_2^- step on FeN_2O_2.

As aforementioned, the M-N_4 structure has a symmetrical electronic density distribution from the coordination of the metal center with four N atoms, which is not conducive to the adsorption and activation of N-intermediates. Based on the recently published studies, introducing intrinsic and heteroatom doping defects is regarded as a better strategy to overcome these obstacles. Xu *et al.* proposed a P-doped Fe-N-C SAC which performed a 90.3% FE_{NH3} at -0.4 V *vs.* RHE. At -0.8 V *vs.* RHE, a partial current density of 110 mA cm^{-2} can be reached for NH_3 production with a yield rate of 18 mg h^{-1} mg_{cat}^{-1}[59]. By replacing partial N to P, the initial Fe-N_4 configuration was broken, optimizing the electronic structure of Fe SACs and facilitating the cathodic charge transfer. As a result, the transformation from NO* to NOH* is easier on the $FeN_3P_1O_1$ surface. Moreover, it could be concluded from the obtained data that the adsorption of intermediates can be controlled by the tuning of P. In this case, Fe-N/P-C SAC exhibited an enhanced NO_3^- adsorption and NO_2^- inhibition capability [Figure 2I and J]. Through a S-doping strategy, Liu *et al.* synthesized ZIF-derived Fe SACs with FeS_1N_3 active centers [Figure 2K and L][60]. The doped S can optimize the symmetry of isolated Fe sites and the electron distribution of Fe. In addition, the interaction between Fe active sites and NO_3^- can also be optimized by doping S. As a result, the S-doped Fe SAC performed a 93.9% FE_{NH3} at -0.47 V *vs.* RHE. Apart from doping heteroatoms to metal centers, defect engineering was also applied to fabricate Fe-SACs. Since the introduction of defects can regulate the electronic structure around

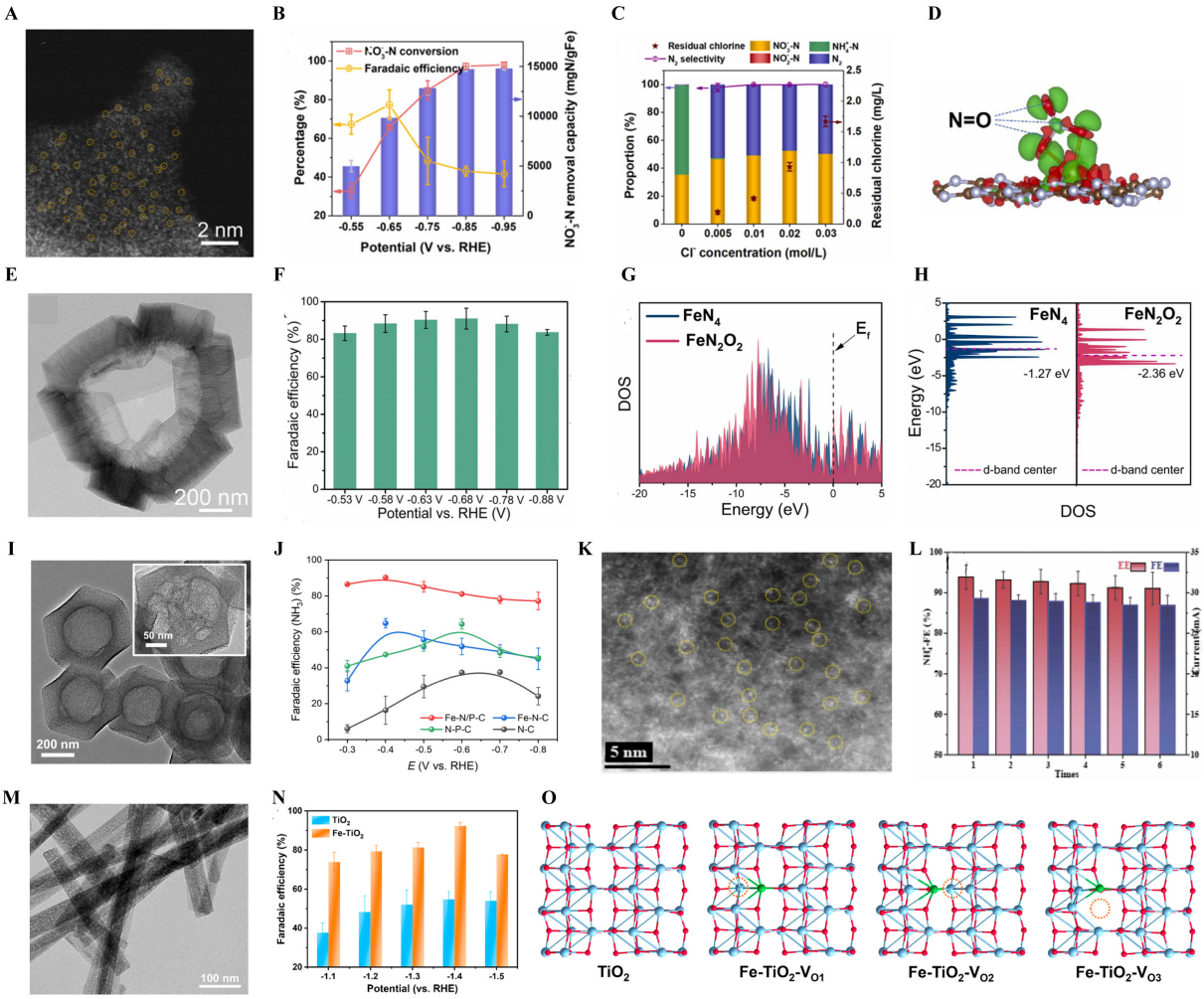

Figure 2. (A) AC-HAADF-STEM image of Fe_{SAs}/g-C_3N_4; (B) The conversion of NO_3^--N and FE of NH_3 using Fe_{SAs}/g-C_3N_4; (C) N product distributions in the presence of chlorine; (D) Differential charge density of NO_3^- adsorbed on Fe_{SAs}/g-C_3N_4. This figure is quoted with permission from Song *et al.*[57]; (E) TEM image of Fe SAC; (F) FE_{NH3} using Fe SAC at different applied potentials; (G) The DOS of the FeN_2O_2 and FeN_4 with Fermi level; (H) The Fe d orbitals of FeN_2O_2 and FeN_4 with d-band center. This figure is quoted with permission from Zhang *et al.*[58]; (I) TEM and enlarged images (Inset) of Fe-N/P-C catalyst; (J) FE_{NH3} of Fe-N/P-C catalyst by applying different working potentials. This figure is quoted with permission from Xu *et al.*[59]; (K) HAADF-STEM image of the S-doped Fe SAC; (L) Cycle FEs and half-cell EEs of S-doped Fe SAC at -0.47 V *vs.* RHE. This figure is quoted with permission from Liu *et al.*[60]; (M) TEM image of Fe-TiO_2; (N) The yield rates of NH_3 generation using Fe-TiO_2 using different working potentials; (O) The optimized structure models of TiO_2 and Fe-doped TiO_2. This figure is quoted with permission from Wang *et al.*[61].

metal ions, Wang *et al.* presented oxygen vacancy-rich Fe-TiO_2 with 92.3% FE_{NH3} and an NH_3 yield rate of 137.3 mg h^{-1} mg_{cat}^{-1} at -1.4 V *vs.* RHE [Figure 2M-O][61]. Given that the active surface is full of anchored positive charged Fe, the HER was effectively suppressed due to the inhibition of protons on the active surface. Moreover, incorporating Fe atoms triggered oxygen vacancy generation on the TiO_2 surface, which optimized the adsorption energy barrier of oxygen-containing intermediates and built an unsaturated coordination structure with abundant active sites.

Other metal SACs

In addition to Fe and Cu SACs, Zn, Ni, Zr, and Co-based SACs are also investigated and gained better NITRR performances. Zhao *et al.* proposed a N-doped carbon-supported Zn SAC (ZnSA-MNC) with microporous structure and achieved 97.2% NO_3^- conversion, 94.9% NH_3 selectivity, 39.27 mg h^{-1} mg_{cat}^{-1} NH_3

yield rate at -1.0 V *vs.* RHE. Meanwhile, a 94.8% FE_{NH_3} can be obtained at -0.9 V *vs.* RHE [Figure 3A-C][62]. The coordination of Zn and N offers Zn sites a positive charge due to the stronger electronegativity of N (3.04) than that of Zn (1.65). As a result, the capture of NO_3^- on Zn active sites was greatly improved by means of the redistribution of charge density. ZnSA-MNC also exhibited a 1.46 eV barrier to avoid the desorption of NO*, which facilitated the follow-up N-end hydrogenation process for NH_3 production. Yang *et al.* synthesized an oxygen vacancies-riched Zr-TiON SAC by anchoring Zr single atoms on a N-doped TiO_{2-x} support[63]. The unsaturated Zr sites can form frustrated Lewis acid-base pairs (FLPS) with the oxygen atoms around the oxygen vacancies [Figure 3D and E]. In the presence of FLPS, NO_3^- tends to adsorb on the Zr sites, while water dissociation can be boosted on the TiON structure. The generated *H was further adsorbed by the oxygens around oxygen vacancies, thus facilitating the hydrogenation process on Zr sites to produce ammonia. As a result, the Zr-TiON SAC performed a 94.8% NH_4^+ Faradaic efficiency and yield rate of 11.28 mg h^{-1} mg_{cat}^{-1} at the current density of -60 mA cm^{-2}. Ni is favorable to adsorb hydrogen species, thus facilitating the hydrogenation process of N-intermediates. Focusing on solitary Ni single atoms and the interactions between B and N of the coordination structure, Ajmal proposed a boron atom-spanning strategy to build a B and N co-doped graphene-supported Ni single atom (NiSA@BNG) for NITRR [Figure 3F and G][64]. By incorporating B in the Ni-N_4 coordination structure, more active sites were obtained in NiSA@BNG, and the electric field generated from the difference of electronegativity between B and N enhanced the capability for nitrate adsorption and greatly improved the performance of the NITRR process. As a result, NiSA@BNG exhibited a 95% NH_4^+ Faradaic efficiency and yield rate of 0.168 mg h^{-1} cm^{-2} at -0.4 V *vs.* RHE. It is difficult to circumvent the regulation of metal-N bonds when constructing and optimizing metal SACs. Li *et al.* developed N-doped carbon basal plane-supported Co SACs for NITRR application[65]. By doping P atoms to the catalyst, they got abundant defects and sites to realize the anchoring process of Co single atoms. The obtained Co SACs displayed a rational CoP_1N_3 coordination structure with a 92% NH_4^+ Faradaic efficiency and 0.433 mg h^{-1} cm^{-2} yield rate at -0.69 V *vs.* RHE [Figure 3H and I]. It could be concluded from the obtained FT- and Wavelet-Transformed (WT)-EXAFS results that the local coordination structure and electron density of the Co-active center can be changed by the doping of P. The P doping enhanced defects, consequently altering the properties of the Co center owing to the strong metal-support interaction (SMSI) effect. As a result, the distribution and stability of anchored Co atoms are greatly improved to facilitate the performance of NITRR.

Single-atom alloys

Alloying active metals with other heterogeneous metals is an effective avenue to improve the performance of catalysts[66-69]. The atomic structure of active sites and the adsorption energy barrier of reactants and intermediates can be optimized through the alloying step. For instance, Wang *et al.* utilized the element Ni to build CuNi alloy catalysts by tuning the molar ratios between Cu and Ni[70]. The $Cu_{50}Ni_{50}$ catalyst exhibits a six-fold activity enhancement than pure Cu at 0 V *vs.* RHE, which can be attributed to the adsorption energy modification by tuning the d-band center of Cu towards the Fermi level[70]. However, the performance of $Cu_{50}Ni_{50}$ is unsatisfactory in lower nitrate concentrations, which can be ascribed to the Ni-Ni coordination induced HER on the catalyst surface. Single-atom alloys (SAAs) are a metal matrix with foreign active metal atoms dispersed across the surface. In this case, the active atoms are diluted in the alloy system, providing a unique electronic structure and geometric characteristics to SAAs. As a result, SAAs may have both unique bimetallic alloying effect and maximum atom-utilization efficiency.

Cu-based materials have excellent $*NO_3$ adsorption capacity. However, the weak *H adsorption on Cu limits the hydrogenation steps and affects the overall performance of NITRR. Accordingly, based on the studies of PdCu and NiCu alloying catalysts, doping metal heteroatoms on the surface of Cu substrates would be a better strategy. Du *et al.* proposed a facet-dependent PdCu SAA by spreading Pd atoms on CuNPs [Figure 4A and B][71]. Given that Pd atoms are uniformly separated, the intercouple of *H was

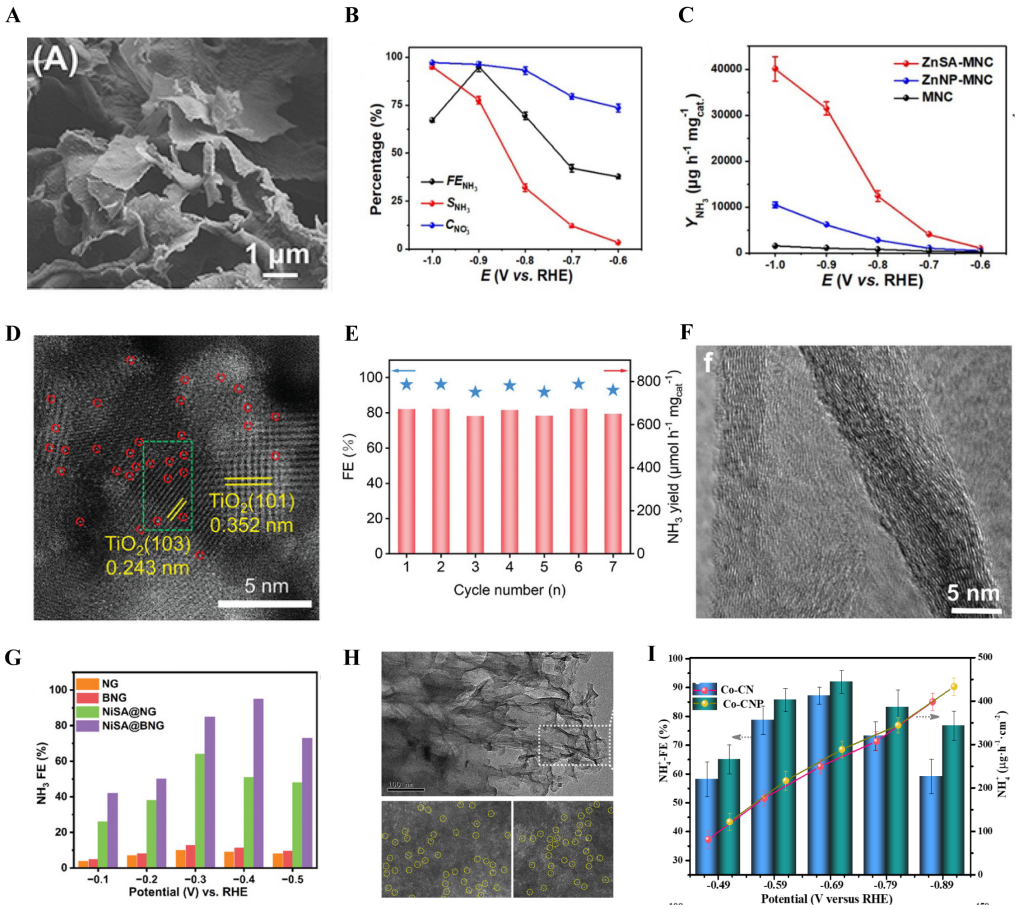

Figure 3. (A) SEM image of ZnSA-MNC; (B) The C_{NO3}^-, S_{NH3}, and FE_{NH3} of ZnSA-MNC at different working potentials; (C) The NH_3 yield of ZnSA-MNC, ZnNP-MNC, and MNC at different working potentials. This figure is quoted with permission from Zhao *et al.*[62]; (D) AC-HAADF-STEM image of Zr-TiON; (E) Stability of Zr-TiON. This figure is quoted with permission from Yang *et al.*[63]; (F) HR-TEM image of NISA@BNG catalyst; (G) FE_{NH3} using NG, BNG, NISA@NG, NISA@BNG as the catalyst. This figure is quoted with permission from Ajmal *et al.*[64]; (H) High-resolution TEM and HAADF-STEM images of Co-CN and Co-CNP; (I) NH_4^+-Faradic efficiency and NH_4^+-yield rate using Co-CN and Co-CNP at different working potentials. This figure is quoted with permission from Li *et al.*[65].

suppressed. Compared to the higher energy barrier of *NOO hydrogenation (0.39 eV) on the Cu (100) facet, the PdCu (100) facet shows a significantly decreased energy barrier of *NHOH (0.10 eV). Consequently, the generated *H intermediates prefer to desorb and react with N-intermediates on the neighboring Cu sites, thus offering PdCu SAAs an ultrahigh 97.1% FE_{NH3} and 0.26 mg h^{-1} cm^{-2} NH_3 yield rate at -0.6 V *vs.* RHE. Similarly, Liu *et al.* alloyed Rh atoms with Cu substrates to overcome the weak *H adsorption on bare Cu. With a low Rh loading (0.6%), the Rh@Cu SAA revealed a partial current density of 162 mA cm^{-2} for NH_3 production with 93% FE_{NH3} and 21.59 mg h^{-1} cm^{-2} NH_3 yield rate at -0.2 V *vs.* RHE[72]. The cooperation between Rh and Cu sites on Rh@Cu SAA comprehensively improves NITRR performances. Based on the computational methods, the *H intermediates are preferred to generate on Rh sites, and Rh active sites play an important role in transferring hydrogen for the N hydrogenation process on Cu sites. Therefore, the free energy of NITRR steps is decreased when Rh atoms are spread on Cu substrates. Cai *et al.* reported a Ni_1Cu SAA by *in-situ* electrochemically incorporating Ni single atoms into a Cu catalyst[73]. They found the alloyed structure of Ni_1Cu exhibited a larger electron cloud than pristine Cu-Cu, which increased the energies of unoccupied anti-bonding N_{2p} states above the Fermi level and inhibited byproducts production from NOOH* intermediates desorption. The addition of Ni significantly reduced the operating potential of the proposed NITRR system, thus weakening the implications of the HER process. At -0.55 V *vs.* RHE, the

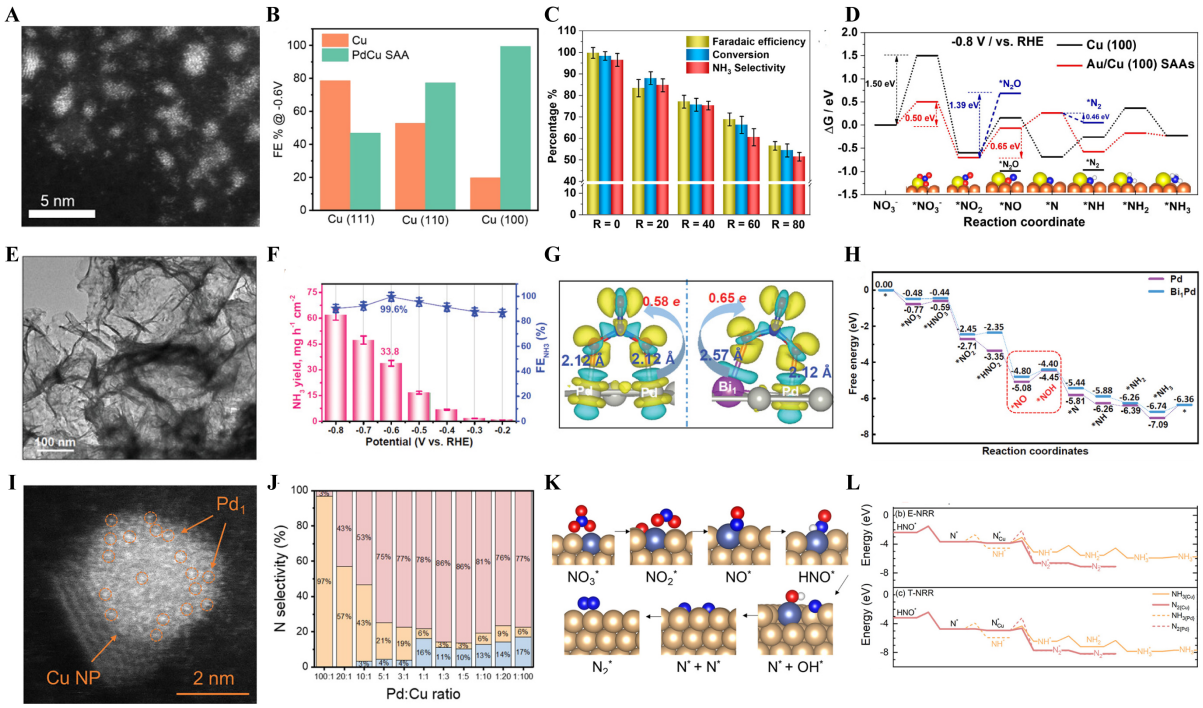

Figure 4. (A) AC-HAADF-STEM image of PdCu SAA; (B) FE_{NH3} of Cu and PdCu SAA. This figure is quoted with permission from Du *et al.*[71]; (C) FE, selectivity and the conversion rate of NITRR process on differentiated Au/Cu SAAs; (D) Free energies for generating different intermediates on Cu (100) and Au/Cu (100) SAAs. This figure is quoted with permission from Yin *et al.*[74]; (E) TEM image of Bi_1Pd; (F) NH_3 yield and FE_{NH3} of Bi_1Pd at various potentials; (G) Charge density difference for $*NO_3^-$ on Pd (left) and Bi_1Pd (right); (H) Free energy diagram of energy-preferred NO_3RR pathways on Pd and Bi_1Pd. This figure is quoted with permission from Chen *et al.*[76]; (I) HAADF image of the Pd/Cu (1:100); (J) product distribution of N_2, NH_4^+, NO_2^- on Pd/Cu(x:y) catalysts; (K) Transformation pathway for NO_3^- reduction to N_2 on Pd/Cu; (L) E-NRR and T-NRR HNO* reduction pathway on Pd_1 and Cu sites. This figure is quoted with permission from Wu *et al.*[78].

proposed system obtained a nearly 100% FE_{NH3}. Compared to the unincorporated Cu catalyst, the Ni_1Cu SAA shows a 10.7 times enhancement of the NH_3 yield rate (5.5539 mg h^{-1} cm^{-2}). In addition, they fabricated a Ni_1Cu SAA-based Zn-nitrate battery with a power density of 12.7 mW cm^{-2} to realize energy output and NH_3 production in a single module.

Yin *et al.* proposed an Au/Cu SAA to combine the advantages of Au SACs and Cu-based catalysts[74]. By anchoring Au atoms on the Cu (100) facet, the NITRR performance was greatly improved on Au/Cu (100) SAAs [Figure 4C and D]. Additionally, incorporating Au single atoms effectively avoids the formation of N_2O and N_2 by tuning the adsorption energies of key intermediates. As a result, Au/Cu (100) SAAs obtained an ~100% FE_{NH3} with a maximum NH_3 yield rate of 3.281 mg h^{-1} cm^{-2} at -0.8 V *vs.* RHE. Combining vacancy engineering with the unique characteristics of SAAs, Zhang *et al.* designed AuCu SAAs by anchoring Au atoms on the Cu (111) nanosheets[75]. By constructing Cu vacancy, the electron transfer capability from Cu to Au sites was greatly improved on V_{Cu}-Au_1Cu SAAs. The evenly distributed Au atoms and Cu vacancies effectively suppressed the HER and generated active hydrogen for promoting the hydrogenation processes in NITRR. As a result, the proposed catalyst shows a 98.7% FE_{NH3} and 0.555 mg h^{-1} cm^{-2} NH_3 yield rate at -0.2 V *vs.* RHE.

While d-block TMs are widely used in fabricating single atom-based catalysts, p-block metals are rarely investigated as active centers for building SAAs. To this end, Chen *et al.* proposed a Pd-supported Bi-SAA (Bi_1Pd) catalyst for NITRR [Figure 4E-H][76]. Depending on the DFT calculations and experimental results,

NO_3^- can be activated on both Pd and Bi_1Pd sites due to the electron transfer and accumulation mechanisms. The alloying between Bi and Pd facilitated the tuning of the energy barrier of the potential determining step of *NO to *NOH and the thermodynamic parameters of NITRR. Benefiting from the less negative binding free energy of *H on Pd and Bi_1Pd surfaces, the *H tends to bind with NO_3^- rather than combine with other *H on the active sites. As a result, an ~100% FE_{NH3} and 33.8 mg h^{-1} cm^{-2} NH_3 yield rate were achieved by the Bi_1Pd catalyst at -0.6 V *vs.* RHE. Xie *et al.* proposed a p-block metal incorporated intermetallic SAA In-Pd bimetallene (ISAA InPdene) for NITRR. The p-d hybridization between Pd and In provides a narrowed energy band, facilitating the rate-limiting step from *NO to *NHO[77]. Benefiting from the intermetallic structures, single atom characteristics, and metalline properties, ISAA InPdene exhibits an 87.2% FE_{NH3} and 28.06 mg h^{-1} cm^{-2} NH_3 yield rate at -0.6 V *vs.* RHE in neutral electrolytes.

In recent studies, most SAAs have focused on transforming NO_3^- to NH_3, while few studies are dedicated to transferring NO_3^- to N_2. In environmental considerations, the N_2 generation pathway would be preferred for water remediation scenarios. To this end, Wu *et al.* developed PdCu alloy catalyst and PdCu SAA for thermo-catalytic and electrocatalytic treatment of NO_3^- towards N_2, respectively [Figure 4I-L][78]. They revealed that PdCu alloys and PdCu SAAs benefit from the thermo-catalytic and electrocatalytic processes, respectively. By changing the molar ratios of Pd and Cu in PdCu alloys and PdCu SAAs, $Pd/Cu_{(3:1)}$ shows great N_2 selectivity (77%) with 19% NH_4^+ selectivity under thermo-catalytic conditions. On the other hand, the N_2 selectivity reached 94% with the capability to suppress HER under electrocatalytic conditions on $Pd/Cu_{(1:100)}$ SAA. The authors investigate the differentiated mechanisms behind the thermo-catalytic and electrocatalytic processes of $Pd/Cu_{(1:100)}$ by DFT calculations. A higher NO_3* stabilization on $Pd/Cu_{(1:100)}$ can be achieved by the electrocatalytic process, while the adsorbed NO_3^- is more likely to desorb into the solution under the thermo-catalytic conditions, thus leading to a higher electrocatalytic NO_3^- reduction activity. Moreover, due to the localized pH effects and proton extraction capability, N*-N* coupling shows a lower formation energy barrier than the *N-*H coupling process on $Pd/Cu_{(1:100)}$ under electrocatalytic conditions. As a result, the electrocatalytic process is conducive to N_2 generation.

SYNTHETIC METHODS OF SACS FOR NITRR

Constructing strong interaction between metal single atoms and supports is a key step to improving the atom-utilization efficiency and the stability of SACs[79]. Typically, impregnation, coordination site construction (MOFs and polymerization stabilized), and defect engineering are the major "bottom-up" strategies for building SACs [Figure 5]. This section summarizes the synthetic methods based on recent advances in SACs-based NITRRs.

Impregnation and coprecipitation strategy

To effectively disperse individual metal atoms onto suitable supports, impregnation and coprecipitation are usually used in synthesizing SACs. Through the impregnation process, metal precursors are uniformly dispersed on the employed support at the initial step. After impregnating for optimal times, the obtained materials will be dried and calcined at high temperatures in the presence of a specific atmosphere. For impregnation strategy, metal loading, precursor selection, and pyrolysis parameters extremely influence the distribution and the performance of metal atoms. Therefore, the optimal chemical environment should be fully investigated during the synthesis.

Xue *et al.* proposed a two-step strategy to prepare Cu MNC-x SAC[49]. To synthesize Cu MNC, SiO_2-coated Cu-ZIF-8 (Cu-ZIF-8@SiO_2) was pyrolyzed at 650 °C in an argon atmosphere, followed by a SiO_2 etching process in NaOH solution. Next, the Cu MNC (650) was reacted with different urea/Cu^{2+} molar ratios in a solution. The urea/Cu^{2+} can adsorb on the pores of Cu MNC (650) and form urea/Cu^{2+}-Cu MNC (650),

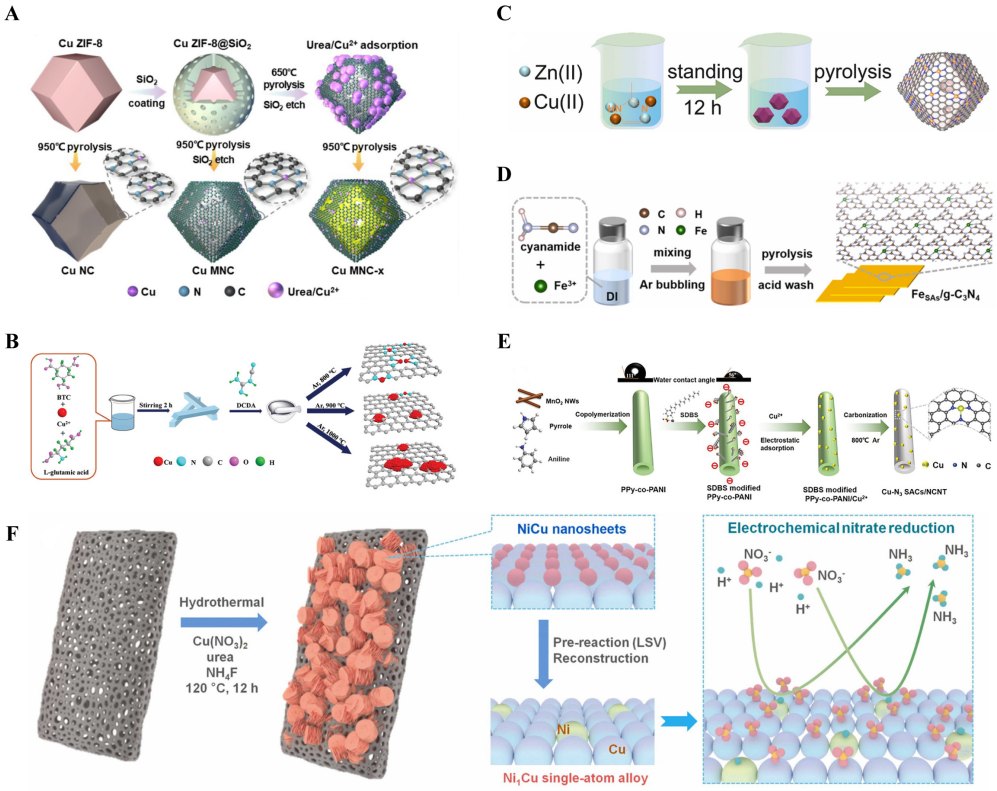

Figure 5. (A) Strategies for synthesizing Cu NC, Cu MNC, and Cu MNC-x. This figure is quoted with permission from Xue *et al.*[49]; (B) Synthesis routes for Cu-N-C-T. This figure is quoted with permission from Zhu *et al.*[47]; (C) Schematic illustration of the synthetic procedure of Cu-N-C. This figure is quoted with permission from Chen *et al.*[41]; (D) Schematic illustration of FeSAs/g-C_3N_4 synthesis. This figure is quoted with permission from Song *et al.*[57]; (E) Strategy for synthesizing Cu-N_3 SACs/NCNT. This figure is quoted with permission from Wang *et al.*[50]; (F) Schematic illustration of the synthesis of Ni_1Cu-SAA. This figure is quoted with permission from Cai *et al.*[73].

which further underwent a pyrolysis process at 950 °C in an argon atmosphere. In the product Cu MNC-x, Cu^{2+} ions can stabilize on the vacancies generated from the evaporated Zn and form stable Cu-N_3-C sites with specific surface area and pore structure to prevent the aggregation of Cu atoms. Yang *et al.* prepared Cu-N-C SAC to investigate the reconstruction of Cu single atoms during the NITRR process[53]. In the initial step, precursors were synthesized by polymerizing 2,6-diaminopyridine on the SiO_2 template. The obtained solid was then pyrolyzed in an NH_3/He gas atmosphere at 800 °C to get SiO_2@N-C. Next, SiO_2 was leached by HF solution, and the remaining product is the N-C support. After impregnating N-C supports by $Cu(NO_3)_2$ solutions, the Cu-doped N-C was further pyrolyzed in a N_2 gas atmosphere at 800 °C to get the Cu-N-C SACs. Yin *et al.* prepared Au/Cu SAAs through a H-spillover method[74]. Using Cu_2O with (100) facets as the support material, ultrapure water dispersed Cu_2O, $HAuCl_4$ solution, and urea were mixed for 3 h at 25 °C. After removing adsorbed urea through a washing step, the formed Au^{3+}/Cu_2O was then treated by the H-spillover process in a H_2/Ar gas atmosphere at 300 °C to get Au/Cu SAAs.

MOFs stabilized SACs

The spatial confinement strategy is an efficient way to construct SACs by immobilizing single atoms on the surface of supports to maximize catalytic efficiency. As a case in point, MOFs show great promise to spatially separate metal atoms in their porous skeletons. Meanwhile, MOFs that contain nitrogen ligands can also provide N and O sites to stabilize metal atoms. Typically, MOF-based SACs undergo a process as follows: (1) the construction of MOFs with specific skeletons; (2) the pyrolysis of MOFs through a programmed thermal treatment process; and (3) the pickling process to remove unwanted metallic residues and impurities using acid.

Zhu *et al.* reported Cu-entrapped nitrogenated carbon nanosheets (Cu-N-C) using Cu-MOFs as the precursor[47]. The Cu-MOF was first prepared by mixing the metal salts and ligands. After drying the collected Cu-MOF, the precipitate was mixed with dicyandiamide and ground into a homogeneous precursor. Subsequently, the precursor was pyrolyzed at 700-1,000 °C in an argon atmosphere. The obtained products were then leached by HCl to remove the unwanted metallic residues. By raising the pyrolysis temperature to 900 °C, the active Cu atoms tend to aggregate and generate CuNPs with weakened NITRR activities, which suggests the pyrolysis temperature is a key factor in influencing the interactions between N sites and metal atoms. Chen *et al.* reported a one-pot ionic exchange method to construct a Cu-N-C structure[41]. Firstly, $Cu(NO_3)_2$, Zn salt and 2-methylimidazole were mixed in methanol and stirred for 12 h at room temperature to get Cu-doped ZIF-8. After pyrolyzing the precipitate at 950 °C in an argon atmosphere, a ZIF-8-shaped porous framework with Cu-N_4 sites was successfully obtained. Zhao *et al.* proposed a similar strategy to stabilize Cu SACs by direct carbonization of Cu-doped ZIF-8[48]. Unlike the strategy by Chen *et al.*, the ligands and Cu salt underwent a hydrothermal process in a Teflon-lined autoclave. After a carbonizing process at 1,000 °C in a N_2 atmosphere, a N-doped porous carbon anchored Cu SAC with Cu-N sites was successfully prepared.

Polymerization stabilized SACs

Polymer materials usually contain N heteroatoms, which is beneficial in supplying coordination sites to build and separate single-atom sites. The polymerization process could employ hard templates, such as MnO_2, SiO_2, and CNTs, to achieve porous structures of catalysts after the pyrolysis and etching processes.

Wang *et al.* prepared Cu-N/P SACs through a template-free oxidative polymerization method[51]. Initially, the pyrrole monomer (C and N sources) and phytic acid (P source) were mixed in an ethanol/water mixture. Next, $CuCl_2$ solution was added to the above mixture to form hydrogel at 4 °C. After the purification and freeze-drying process, the powder was further pyrolyzed in an argon gas atmosphere at 800 °C and underwent a pickling process to get P-doped Cu-N SACs. Song *et al.* proposed a polymerization-pyrolysis method to fabricate Fe_{SAs}/g-C_3N_4[57]. Initially, cyanamide and $Fe(NO_3)_3$ were mixed and sonicated for 1 h. After a pretreatment by argon gas, the solution was treated in a muffle furnace for 1 h at 550 °C. Finally, the unstable metals in Fe_{SAs}/g-C_3N_4 were removed by HCl leaching.

Using CNTs as the hard template, Zhao *et al.* further improved the performance of BCN@Cu SACs in the NITRR process[46]. Initially, CNTs were added to the mixture of 1,10-phenanthroline and Cu salt solution. The mixture solution was then sonicated for 30 min to obtain a metal boron cluster organic polymer (MBOP)/CNT precursor. After a pyrolysis process at 1,000 °C, MBOP/CNT was converted to the BCN@Cu/CNT and achieved greater conductivity and NITRR activity than BCN@Cu. Wang *et al.* proposed Cu-N_3 SACs/NCNT through a polymerization-surface modification-electrostatic adsorption-carbonization strategy. Firstly, pyrrole and aniline were polymerized on the surface of MnO_2 nanowires, which generated N-rich polymer PPy-co-PANI with hollow structures. The surface of the obtained poly(pyrrole-co-aniline) (PPy-co-PANI) was further modified by sodium dodecyl benzene sulfonate (SDBS) to modify its surface charge state and wettability. Since the surface of SDBS-modified PPy-co-PANI is more hydrophilic, Cu^{2+} ions were more likely to adsorb on PPy-co-PANI through the electrostatic attraction. After the carbonization at 800 °C in an argon gas atmosphere, the Cu-N_3 SACs/NCNT was successfully prepared. Wu *et al.* prepared Fe SACs through the polymerization-pyrolysis process using SiO_2 as the hard template[56]. *o*-phenylenediamine, $FeCl_3$, and SiO_2 powder were initially mixed into isopropyl alcohol and stirred for 12 h. The mixture was dried to a solid state through a rotary evaporator, following pyrolysis in an

argon gas atmosphere at 800 °C. Finally, the as-prepared product was leached by alkaline and acid to remove the SiO_2 template and poorly cooperated metals to get Fe SAC.

Defects stabilized SACs and SAAs

Defects engineering of support materials is an emerging approach to optimize catalyst performance and build SACs with unsaturated structures. The defects on the support can be vacancies, interstitial atoms, or substitutional atoms. Introducing defects on the support materials can affect charge density at the active sites, thus influencing the stability and reactivity of SACs.

Wang *et al.* prepared Fe-TiO_2 SACs with interfacial defect by incorporating Fe atoms on the TiO_2 support through adsorption and subsequent reduction strategy[61]. Firstly, the as-prepared TiO_2 nanowire and iron acetylacetonate were added into a CH_3CN solution and stirred for 12 h. After washing and drying the obtained suspension, the solid was then calcined in an Ar/H_2 gas atmosphere at 350 °C to get Fe-TiO_2 SACs. Du *et al.* proposed PdCu SAA by the galvanic replacement of partial Cu atoms to Pd atoms. At the initial step, CuNPs were deposited on the carbon paper through an electrochemical process under the potential of -0.3 V *vs.* Ag/AgCl[71]. Subsequently, carbon paper containing CuNPs was further immersed into a Na_2PdCl_4 solution. The galvanic replacement reaction was spontaneously driven due to the differences of reduction potential between Cu and Pd. After the washing and drying, PdCu SAA was successfully obtained on the carbon paper. Similar approaches are also applied by Liu *et al.* to build Rh@Cu SAA[72]. To build NiCu-SAA, Cai *et al.* immersed a piece of Ni foam into a solution containing $Cu(NO_3)_2$, NH_4F, and urea, following a hydrothermal synthesis process[73]. After washing and drying steps, the obtained NiCu oxide or hydroxide nanosheet catalyst (NiCu-NS) foam material underwent an *in-situ* electrochemical reconstruction to get NiCu-SAA. Zhang *et al.* designed V_{Cu}-Au_1Cu SAAs by combining galvanic replacement and vacancy engineering strategies[75]. For the galvanic replacement, an aqueous solution of $HAuCl_4$ was added dropwise to the HCl solution containing CuNS. The mixture was then thermal treated at 100 °C for 20 min. After filtration, washing, and drying steps, Au_1Cu SAAs were obtained. To get vacancy-engineered SAAs, these SAAs were then immersed into the acetic acid solution and thermal treated at 60 °C for 1 h.

In addition to the above strategies, the microwave-assisted, atomic layer deposition, chemical vapor deposition, and other methods are also efficient for building SACs[80-82]. Combining the further quantification of ammonia and other byproducts in NITRR, these strategies provide opportunities to realize high-performance NITRR processes in future applications.

METHODS FOR AMMONIA AND BYPRODUCTS QUANTIFICATION

Quantifying ammonia and byproducts is beneficial for determining the validity of SACs in the NITRR processes. To ensure accurate results, a combination of different quantification methods is suggested.

Nessler's reagent method for ammonia quantification

The colorimetric quantification of ammonia by Nessler's reagent is based on the reaction between ammonia and mercury(II) ions in an alkaline medium[83].

$$2K_2HgI_4 + NH_3 + 3KOH \rightarrow HgOHg(NH_2)I\downarrow + 7KI + 2H_2O$$

After stabilizing for a few minutes, the yellow-brown $HgOHg(NH_2)I$ complex shows characteristic absorbance at the wavelength between 410 and 425 nm. By plotting a calibration curve through the standard ammonia solutions with known concentrations, the concentrations of ammonia in unknown samples can be detected. Given that mercury ions are present in Nessler's reagent, experimental rules must be strictly

followed during the storage and use process to avoid hazards caused by mercury ingestion. Recently, portable equipment for ammonia testing has also been developed based on Nessler's reagent method, which avoids the inaccurate results caused by ammonia volatilization.

Indophenol method for ammonia quantification

Indophenol is another widely used colorimetric technique for quantifying ammonia in aqueous solutions[84]. Under alkaline conditions, the reaction between ammonia, sodium hypochlorite, and phenol tends to form an indophenol complex, with color changing from yellow to blue. The indophenol blue complex shows characteristic absorbance at the wavelength between 630 and 660 nm. In recent studies, phenol is replaced by sodium salicylate to reduce the output of phenol waste from the colorimetric test. Similarly, the reaction between ammonia, sodium hypochlorite, and sodium salicylate also generates complexes with characteristic absorbance at the wavelength between 630 and 660 nm. By establishing a calibration curve, the concentrations of ammonia in unknown samples can be detected by the spectrophotometric measurements.

^{1}H NMR method for ammonia quantification

The proton nuclear magnetic resonance (^{1}H NMR) method can also quantify ammonia in various samples[85]. By choosing suitable solvents such as D_2O with a standard compound (e.g., dimethyl sulfoxide (DMSO)), the unique proton signals in the spectrum will show typical triple peaks of $^{14}NH_4^+$ and double peaks of $^{15}NH_4^+$ around 7-8 ppm. A calibration curve can be generated according to the peak area from samples with known ammonia concentrations.

Naphthalene ethylenediamine hydrochloride method for nitrite quantification

In this method, *p*-aminobenzene-sulfonamide, N-(1-Naphthyl) ethylenediamine dihydrochloride, and phosphoric acid were mixed to obtain a color reagent with acidic micro-environment[86]. After adding the color reagent to the nitrite-containing solutions, naphthalene ethylenediamine reacts with nitrite ions to form a purple diazonium salt with a characteristic absorbance at a wavelength of around 540 nm. A calibration curve allows the detection of nitrite concentrations in unknown samples through spectrophotometric measurements.

1,10-phenanthroline method for hydroxylamine quantification

The 1,10-phenanthroline method relies on the formation of Fe^{2+} from the reaction between Fe^{3+} and hydroxylamine[87]. Subsequently, 1,10-phenanthroline tends to react with Fe^{2+} and form a ferrous complex, which shows characteristic absorbance at the wavelength around 510 nm. Similarly, by establishing a calibration curve, spectrophotometric measurements can detect the concentrations of hydroxylamine in unknown samples.

TECHNIQUES FOR SACS-BASED NITRR CHARACTERIZATION

Characterizations are crucial to reveal the intrinsic mechanism of SACs in NITRR. Accompanied by experimental results, the comprehensive combination of characterization techniques will guide us in finding an optimal way to enhance the performance of the SACs-based NITRR system. In addition to regular X-ray diffraction (XRD), Scanning Electron Microscope (SEM), Transmission Electron Microscope (TEM), Fourier Transform infrared spectroscopy (FTIR), Ultraviolet-visible (UV-vis) absorption spectra, and X-ray Photoelectron Spectroscopy (XPS) techniques, the emerging approaches can provide in-depth insights to the relevant reaction kinetics during the NITRR process, thus obtaining actual active sites and mechanisms[88].

Aberration-corrected high-angle/medium-angle annular dark-field scanning transmission electron microscopy (AC-HAADF-STEM) offers capabilities for observing the precise locations and microenvironments of materials supported by single atoms, which allows researchers to identify the atomic metal dispersion through the bright spots in the HAADF-STEM images[89]. The AC-HAADF-STEM provides information in distinguishing different element species in the atom-support composites. Through the AC-HAADF-STEM images, the arrangement of single atoms and their interaction with the support material will be recognized[90]. Scanning tunneling microscopes (STM) are another effective tool to characterize surface geometric and electronic structures of SACs at atomic resolution and provide insights into single-atom catalysis[91]. In STM, the topographical and electronic differences of metals can be discerned and exhibited different corrugations under certain tip conditions. Therefore, the bright protrusions of single atoms can be observed and distinguished from their supports. In addition, STM can reveal the interactions between single atoms and coordinative sites, facilitating the understanding of adsorption capability in different local coordination environments. Since structural evolution is also a key parameter for SACs-based reactions, the environmental TEM (ETEM) was developed for *in-situ* monitoring dynamics and atomic structural transformations of single atoms during actual chemical reactions[92].

In addition to these direct observation methods, XAS is also a powerful tool to investigate the electronic structure and coordination structures of SACs [Figure 6A-C][56]. In general, the XAS technique can be divided into XANES and extended XAFS (EXAFS) spectroscopy based on the differences of obtained information[93]. The XANES technique determines the electronic state and the valence of active centers, while EXAFS provides abundant information for coordination elements, coordination number, bond length, debye-waller factor, *etc.* Wu *et al.* performed XAS analysis on the Fe SACs during the NITRR process[56]. Through XANES measurements, they found the oxidation state of Fe sites is between 0 and +3 valence. Additionally, the EXAFS results illustrate the existence of Fe-N coordination and the absence of Fe-Fe coordination. As a further extension of XAS technology, the operando XAS strategy provides an opportunity to monitor the dynamic behavior of geometric structure of SACs and electronic environment during the catalysis process[93]. At the atomic scale, the structural evolution of metal-N_x sites can be monitored according to the peak shifts of the EXAFS spectrum.

Operando synchrotron radiation (SR)-FTIR spectroscopy is another powerful tool that reveals the reaction pathway by observing key intermediates during the reaction. Typically, NO_3^- shows a negative band at around 1,360 cm^{-1}, while the *NO, *NO_2, NH_2, *NH_2OH, and the produced NH_4^+ correspond to the positive bands at around 1,580, 1,230, 1,270, 1,150, and 1,460 cm^{-1}, respectively[94]. For instance, Xu *et al.* utilized operando SR-FTIR to monitor the intermediates of NITRR when using Fe-N/P-C SAC as the catalyst. By varying operation potentials from 0 to -0.8 V *vs.* RHE, an increased peak intensity of NO_3^- was observed at 1,390 cm^{-1}, which can be attributed to the continuous consumption of NO_3^- on the active sites. Furthermore, the NO_2^- stretching mode peak at 1,290 cm^{-1} indicates a deoxygenation step occurred during the NO_3^- reduction, providing strong evidence for their proposed reaction pathways [Figure 6D and E][59].

Additionally, the online DEMS efficiently monitors the intermediates during the NITRR process [Figure 6F and G]. The generated intermediates are convenient to be qualitative and quantitative by sorting their mass-to-charge ratio in the mass spectrometry[72]. As a result, the reaction pathway of the proposed system can be explicitly investigated. Moreover, the electron paramagnetic resonance (EPR) method efficiently identifies hydrogenation steps by capturing H* with 5,5-dimethyl-1-pyrroline-N-oxide (DMPO, Figure 6H and I)[75]. Using the EPR technique, Zhang *et al.* have pointed out a decreased DMPO-H characteristic peak with increasing NO_3^- concentrations, indicating the hydrogenation between H* and N-intermediates is before DMPO capture and the H-H coupling process[75]. Therefore, combining different characterization methods is conducive to revealing the rational material structure and NITRR pathways.

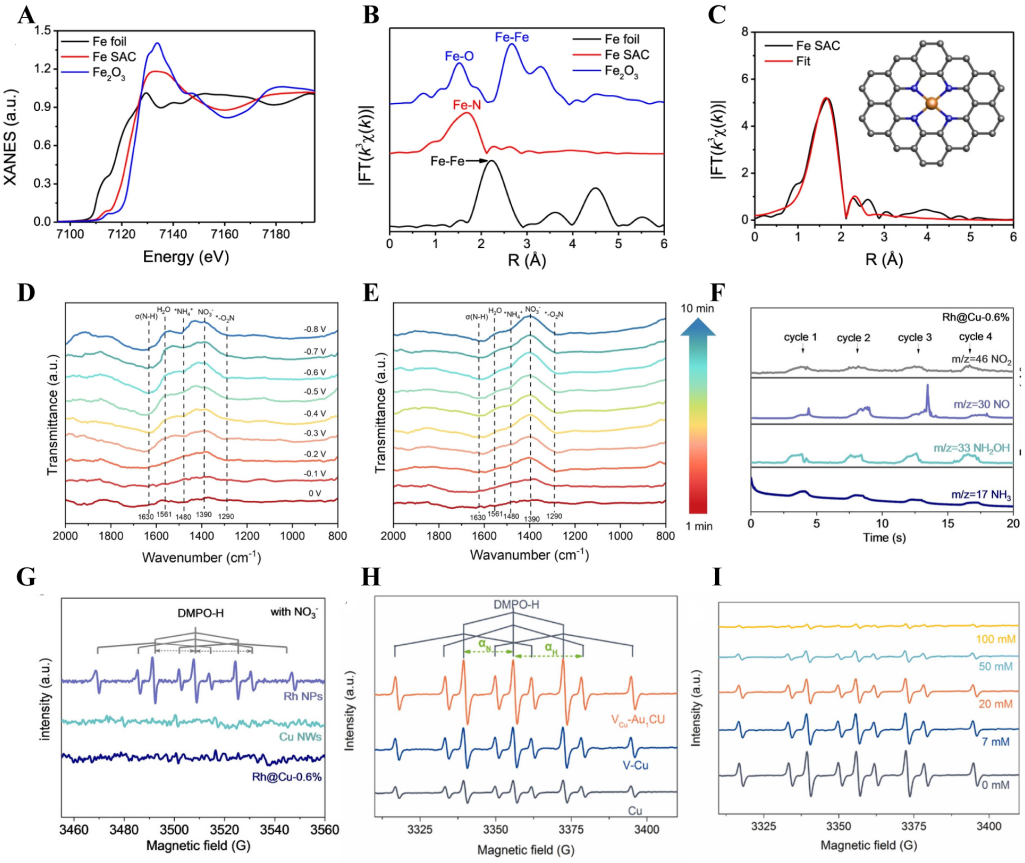

Figure 6. (A) The XANE spectra of Fe SAC, Fe foil and Fe_2O_3 at Fe K-edge; (B) FT k^3-weighted χ(k)-function of the EXAFS spectra at Fe K-edge; (C) XANES spectrum of Fe SAC at Fe L-edge. This figure is quoted with permission from Wu *et al.*[56]; (D) Operando SR-FTIR spectra of Fe-N/P-C catalyst during NITRR process; (E) Time-dependent planar SR-FTIR spectra (-0.4 V *vs.* RHE). This figure is quoted with permission from Xu *et al.*[59]; (F) EPR spectra of Cu NWs, Rh@Cu-0.6% and Rh NPs based NITRR systems at -0.1 V *vs.* RHE (react for 3 min); (G) DEMS measurements of NITRR using Rh@Cu-0.6% as the catalyst. This figure is quoted with permission from Liu *et al.*[72]; (H) EPR signals of DMPO-H from the NITRR system using Cu NSs, V-Cu NSs and VCu-Au_1Cu SAAs as the catalyst; (I) EPR signals of DMPO spin adducts from the NITRR system using VCu-Au_1Cu SAAs as the catalyst. This figure is quoted with permission from Zhang *et al.*[75].

MECHANISMS OF SACS-BASED NITRR

Electrochemical NO_3^- remediation requires complex steps to obtain the target products (NH_3 and N_2). Accordingly, various by-products (NO_2^-, N_2O, NO, NH_2OH, and N_2H_4) will be generated to adverse the performance of NITRR[95]. Based on the existing studies, remediating NO_3^- to N_2 undergoes a 12 protons and ten electrons transfer process, while NO_3^- to NH_3 involves nine protons and eight electrons transfer[96].

$$2NO_3^- + 12H^+ + 10e^- \rightarrow N_2 + 6H_2O \quad E^0 = 1.17 \text{ V } \textit{vs.} \text{ SHE}$$

$$NO_3^- + 9H^+ + 8e^- \rightarrow NH_3 + 3H_2O \quad E^0 = -0.12 \text{ V } \textit{vs.} \text{ SHE}$$

In the initial steps of NITRR, the adsorption of NO_3^- plays a vital role in influencing its activity and selectivity. Since NO_3^- can adsorb to active sites *via* chemisorption (2-O and 1-O) and physisorption, Wang *et al.* investigated the adsorption mode of NO_3^- by taking Cu (111) surface as an example[97]. The study revealed that NO_3^- is preferred to adsorb on the Cu (111) via the 2O mode (Gibbs free energy = -0.1 eV) rather than the 1O mode (Gibbs free energy = 0.14 eV). Additionally, they

identified seven TM-Cu (111) candidates with negative valued ΔG_{*NO3}, which can suppress HER and lead to a desired NITRR selectivity [Figure 7A and B].

Unlike the less selective N-N coupling for N_2 formation, forming NH_3 involves four varied mechanisms (O-end, O-side, N-end, and N-side) based on the adsorption mode of NO* intermediate on the active sites[97-99]. Through the computational studies, the TM-graphitic carbon nitride (g-CN) SACs and TM-SAAs favor a N-end adsorption. Meanwhile, the reasonable pathway (O-side, N-side, and N-end) for TM-N_4 SACs needs to be determined by the anchored TM atom types. Moreover, calculating limiting potentials (U_L) for NH_3 production effectively evaluates the activity of different metal centers. After calculating the U_L of 20 different TM centers, Niu *et al.* pointed out that Ti/g-CN and Zr/g-CN exhibited low U_L of -0.39 and -0.41 V *vs.* RHE, respectively[98]. This indicated that Ti/g-CN and Zr/g-CN catalysts will show better performances in NITRR [Figure 7C and D]. By exchanging nitrogenated holey-doped graphene (g-C_2N) as a single-atom substrate, Zhu *et al.* investigated the potential catalytic performance of TM-G_2N. Accordingly, Zr/g-C_2N and Hf/C_2N show better performance for generating NH_3 in NITRR with low U_L of -0.28 and -0.27 V *vs.* RHE, respectively [Figure 7E][99]. For SAAs, Wang *et al.* provided theoretical guides for constructing TM-based SAAs on the Cu (111) surface. Among the 27 kinds of SAAs, Ni/Cu (111) shows the best performance in NITRR with U_L of -0.29 V *vs.* RHE[97]. A reasonable NITRR pathway can be concluded as: (1) the adsorption of NO_3^-; (2) simultaneous generation of active hydrogen; (3) hydrogenation of $*NO_3$ to form $*NO_2$ and *NO; (4) differentiated *NO adsorption mode based on the active site types; and (5) continuous hydrogenation to the target products of NH_3 and N_2. However, N-N coupling is thermodynamically unfavored to occur on the single sites of SACs, leading to NH_3 as the final product in most studies.

CONCLUSION AND OUTLOOK

Electrochemical NITRR process has been proven to be a green and sustainable approach for NO_3^- remediation and NH_3 production. Designing catalysts with fine electron structure, stability, high atomic utilization, and activity are the primary tasks to improve the performance of NITRR. This review systematically generalizes the recent advances in the field of NITRR dependent on SACs. Apparently, SACs have exhibited great potential in NITRR due to their maximum atom-utilization efficiency, fully exposed active sites, and unique electronic properties. Currently, it remains challenging to achieve large-scale production and commercial applications of SACs. Given that most fundamental research ultimately aims to serve social production, the practical application of SACs-based NITRR still has a long way to meet the standards since current research remains at the laboratory scale.

Inhibiting the aggregation and migration of single atoms

Despite great efforts to enhance the NITRR performances in recent SACs-based strategies, the yield rate of NH_3 remains lower due to the limited number of active sites [Table 1]. From an application viewpoint, ensuring a high dispersion of isolated single atoms on SACs is urgent to maximize catalytic activity. However, the atomic scale sites imply the greatly increased free energy of the single atoms. The mass loading of single atoms may induce inevitable migration and aggregation and generate unfavored clusters/nanoparticles under large overpotentials[100]. Once the advantage structure was destroyed, the production of unwanted N-byproducts and H_2 would dominate the NITRR process, adversely affecting the stability of SACs. Since the stability of SACs is vital for determining their large-scale applicability and commercial viability, it should be considered as an important indicator during the electrocatalytic process. To improve it, strong binding energy between single-atom sites and substrates is beneficial to prevent the migration or aggregation of single atoms[101]. By optimizing the binding energy through surface modification and changing suitable support materials, migration and aggregation are expected to be effectively

Table 1. Summary of catalytic performance of SACs in NITRR

SACs	Operation voltage	FE %	Electrolyte	NH_3 yield rate	Stability (cycle)	Durability (h)	Ref.
BCN@Cu	-0.6 V *vs.* RHE	97.37	KOH + NO_3^-	83.95 mg h^{-1} mg_{cat}^{-1}	10	16	[45]
BCN@Cu/CNT	-0.6V *vs.* RHE	95.32	KOH + NO_3^-	172.227 mg h^{-1} mg_{cat}^{-1}	10	N/A	[46]
Cu-N-C	-1.5 V *vs.* SCE	94	Na_2SO_4 + NO_3^-	0.25 mg h^{-1} mg_{cat}^{-1}	8	N/A	[41]
Cu_{SA}NPC	-1.1 V *vs.* RHE	87.2	PBS + $NaNO_3$	5.204 mg h^{-1} mg_{cat}^{-1}	10	N/A	[48]
Cu MNC	-0.64 V *vs.* RHE	52.0	Na_2SO_4 + NO_3^-	92.922 mg h^{-1} mg_{cat}^{-1}	14	84	[49]
Cu-N_3 SACs/NCNT	-0.8 V *vs.* RHE	89.64	KOH + KNO_3	30.09 mg h^{-1} mg_{cat}^{-1}	10	N/A	[50]
Cu-N_4/P	-0.6 V *vs.* RHE	95.89	Na_2SO_4 + $NaNO_3$	2.01 mg h^{-1} mg_{cat}^{-1}	6	N/A	[51]
Cu SAA	-0.9 V *vs.* RHE	87.0	Na_2SO_4 + NO_3^-	0.3 mg h^{-1} cm^{-2}	20	~300	[52]
FeN_4 SAC	-0.66 V *vs.* RHE	~75	KNO_3 + K_2SO_4	20 mg h^{-1} mg_{cat}^{-1}	20	N/A	[56]
Fe/g-C_3N_4	-0.65 V *vs.* RHE	77.3	Na_2SO_4 + NO_3^-	N/A	8	N/A	[57]
FeN_2O_2-SAC	-0.66 V *vs.* RHE	~92	KNO_3 + K_2SO_4	46 mg h^{-1} mg_{cat}^{-1}	15	N/A	[58]
Fe-N/P-C	-0.8 V *vs.* RHE	90.3	KOH + KNO_3	18 mg h^{-1} mg_{cat}^{-1}	20	N/A	[59]
S-doped Fe SAC	-0.47 V *vs.* RHE	93.9	Na_2SO_4 + $NaNO_3$	N/A	6	N/A	[60]
Fe-TiO_2	-1.4 V *vs.* RHE	92.3	KNO_3 + K_2SO_4	137.3 mg h^{-1} mg_{cat}^{-1}	5	N/A	[61]
Zn-SAC	-1.0 V *vs.* RHE	94.8	Na_2SO_4 + $NaNO_3$	39.27 mg h^{-1} mg_{cat}^{-1}	20	N/A	[62]
Zr-TiON	N/A	94.8	Na_2SO_4 + KNO_3	11.28 mg h^{-1} mg_{cat}^{-1}	7	14	[63]
NiSA-BNG	-0.4 V *vs.* RHE	95	Na_2SO_4 + $NaNO_3$	0.168 mg h^{-1} cm^{-2}	5	N/A	[64]
Co-SAC	-0.69 V *vs.* RHE	92.0	Na_2SO_4 + NO_3^-	0.4333 mg h^{-1} mg_{cat}^{-1}	5	N/A	[65]
PdCu-SAA	-0.6 V *vs.* RHE	97.1	Na_2SO_4	0.26 mg h^{-1} mg_{cat}^{-1}	N/A	10	[71]
Rh@Cu	-0.2 V *vs.* RHE	93	Na_2SO_4 + KNO_3	21.59 mg h^{-1} cm^{-2}	N/A	30	[72]
Ni_1Cu-SAA	-0.55 V *vs.* RHE	~100	K_2SO4 + NO_3^-	5.554 mg h^{-1} cm^{-2}	N/A	N/A	[73]
Au/Cu SAAs	-0.8 V *vs.* RHE	99.69	$NaNO_3$ + Na_2SO_4	3.281 mg h^{-1} cm^{-2}	20	N/A	[74]
V_{Cu}-Au_1Cu SAAs	-0.2 V *vs.* RHE	98.7	KOH + KNO_3	0.555 mg h^{-1} cm^{-2}	5	15	[75]
Bi_1Pd SAAs	-0.6 V *vs.* RHE	99.6	KOH + NO_3^-	33.8 mg h^{-1} cm^{-2}	10	20	[76]
ISAA In–Pd	-0.6 V *vs.* RHE	87.2	$NaNO_3$ + Na_2SO_4	28.06 mg h^{-1} mg_{cat}^{-1}	20	100	[77]

suppressed[19,102]. In addition, it is urgent to propose a unified standard to guide the long-term performance testing of SACs. Continuously monitoring catalytic activity, selectivity, energy efficiency, and structural integrity over extended periods is needed to judge the comprehensive performance of SACs-based electrocatalytic systems. Therefore, the structure evolution of SACs is suggested to be investigated during the NITRR process in future studies. The rational use of operando techniques can help us to track the actual active sites and intermediates, which is beneficial to understanding the structure-activity relationship and the in-depth mechanisms to fabricate more efficient SACs.

Fabrication of SACs with asymmetry active centers

For most inorganic carrier-supported SACs, metal centers are coordinated with four N atoms to form a C_{4V} coordination symmetry. However, recent studies indicate that the symmetrical electronic density distribution shows a weak polar active site, leading to a weak adsorption energy of NO_3^- and intermediates. As a result, the unwanted intermediates are accumulated in the NITRR system and are adverse to the N-pollutant treatment and NH_3 production. The breaking of single-atom symmetry provides a promising approach to adjusting the electronic density of active sites, reducing the energy barrier for forming key intermediates, and strengthening the adsorption energies between actives and N-intermediates. Therefore, the efficient methodologies and in-depth mechanisms for constructing asymmetry active sites urgently need to be investigated based on substrate engineering, heteroatom doping, and defect engineering approaches.

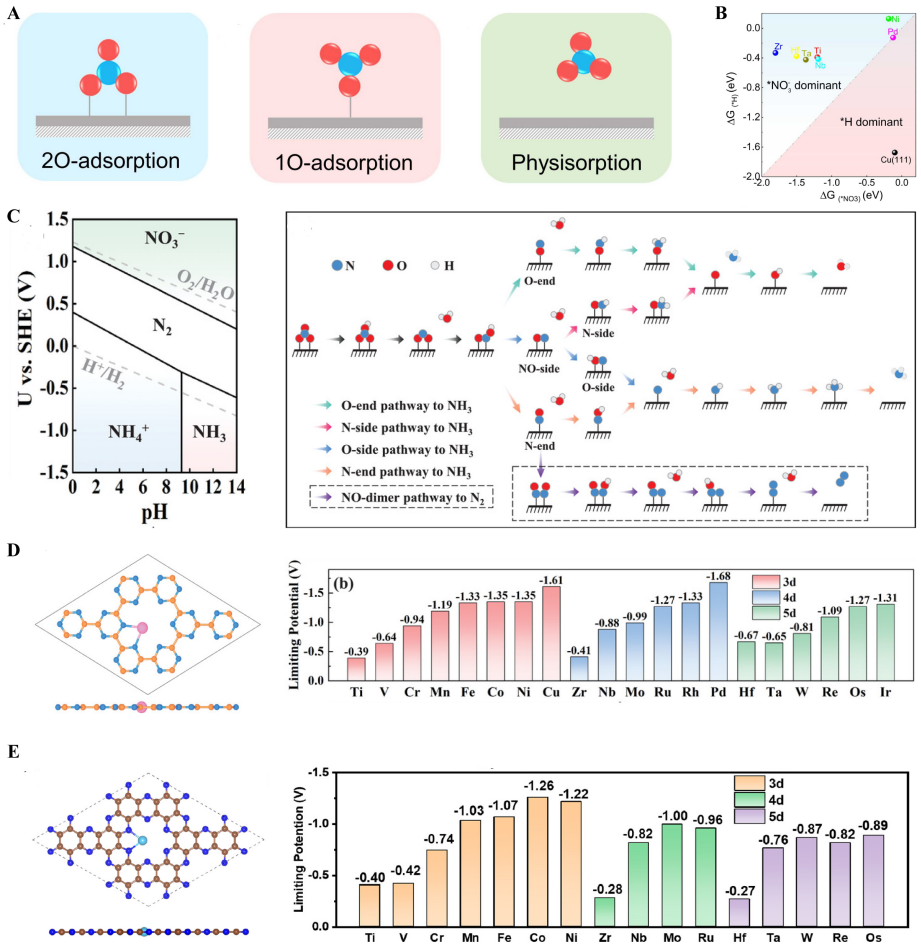

Figure 7. (A) Possible mechanisms for the adsorption of NO_3^- on Cu (111); (B) Calculated ΔG(*NO_3) and ΔG(*H). This figure is quoted with permission from Wang *et al.*[97]; (C) Pourbaix diagram of nitrogen species (left), detailed O-end, O-side, N-end, and N-side pathways to form NH_3, and the NO-dimer pathway to form N_2 (right); (D) Atomic structure of TM/g-CN (left), TM/g-CN limiting potentials for NITRR via the N-end pathway (right). This figure is quoted with permission from Niu *et al.*[98]; (E) The atomic structure of TM/g-C_2N (left), limiting potentials of TM/g-C_2N (right). This figure is quoted with permission from Zhu *et al.*[99].

Optimization of costs

It can be stated that the effective dispersion of single atoms on supports brings cost advantages for synthesizing SACs. However, it is theoretically feasible and faces many difficulties in practical operations. Firstly, maintaining the high performance and uniformity of active sites is a great challenge when performing large-scale synthesis of SACs. The surface conditions of employed supports are generally more complex than expected. Since the coordination atoms will greatly affect the electronic structure of the active sites, it is essential to fully consider the impacts of the amplified system on the coordination atoms before large-scale synthesis of SACs, thus avoiding the incorrect expression of active sites. Therefore, scalable technologies are urgently needed to precisely regulate the microenvironment of the catalyst at the atomic level. On the other hand, most SAC synthesis strategies involve support/precursor preparation, pyrolysis, and further washing/pickling steps. The cost issues caused by these complex synthesis processes will be further magnified in the scale-up SAC synthesis process.

Technical aspects for SACs-based NITRR

A deeper understanding of detailed technical aspects can help us achieve a more efficient ammonia synthesis. In addition to the stability of isolated active sites and cost issues, the atom selection, atom loading,

and reaction environments (pH values, temperature, local pressure, nitrate concentrations, alkaline cations) are also important in designing efficient SACs. To verify the validity of SACs for further water cleaning applications, it is recommended that tests be conducted under conditions that closely mimic practical applications. Generally, heavy metal ions and organic molecules commonly coexist with nitrates in wastewater, which will induce devastating effects on the single-atom active sites by forming strong bonds with active sites. However, current studies generally focus on improving the performance of SACs, little attention was paid to the influences of these unfavorable factors. In addition to the common indicators, the resistant capability of SACs to heavy metal ions and organic macromolecules is recommended as a benchmark in future studies. Furthermore, after obtaining an optimal SAC, the coating of catalysts on electrodes is another key step to ensure the performance of NITRR. Currently, the most widely employed strategy is to prepare a homogeneous catalyst ink and drop the ink onto the electrode. To ensure the uniformity of coated SACs, it is suggested that an airbrush be employed to disperse the homogeneous catalyst ink on the electrode. Additionally, when considering the scale-up application of SACs-based NITRR systems, energy efficiency is another crucial factor. Current strategies majorly focus on the faradaic efficiency and the yield (corresponding to the current density) of target products, while the working potential of proposed systems has always been overlooked. Since the overpotentials in scale-up applications are often larger than those in laboratory-grade cells, it is necessary to optimize reaction conditions and catalyst design to obtain improved energy efficiencies of catalysts.

Theoretical screening for effective SACs configuration

In addition to the experimental investigations, theoretical prescreening is also a powerful route to optimize the fine structures of SACs. Through the modularized DFT simulations, the adsorption of NO_3^-, reaction pathways, thermodynamic Gibbs free energy changes, kinetic activation energy and limiting potentials of different active sites can be estimated. On the other hand, identifying the rate-determining step helps clarify the physicochemical origin of NITRR performances. The theoretical prescreening can drastically reduce the expended efforts of time-consuming experimental screenings. Typically, solving the Schrödinger equation can accurately predict various properties of relevant systems, while the DFT simulation can only provide an approximate result in larger models that contain more atoms[103]. The results of DFT simulations strongly depend on the expression of the employed exchange-correlation (ec) functional[104]. In current SACs-based studies, Perdew-Burke-Ernzerhof (PBE) ec functional is the most widely used method within the generalized gradient approximation (GGA)[56,61,62,71]. However, the accuracy of DFT simulations in most SACs-based studies may deviate from reality since they barely considered the effects of solvent environments (solvation and electrolyte), potentials, and local pH values. In water solvent-based electrochemical processes, the hydrogen bonds, dynamic effects, and secondary interactions with specific directionality cannot be ignored. For the potential and local pH values, it is necessary to consider the extra charges caused by protons in water solvent and electrons on the electrode when constructing models. In the NITRR process, the methodology development of DFT simulations should focus on several critical steps and considerations, including functional, basis set, pseudopotentials, integration grids, spin polarization, validation and benchmark, convergence criteria, and error analysis. The DFT simulation of SACs-based NITRR systems can reference the experiences from other known systems. For instance, the explicit water layer and implicit solvation can be an effective strategy for treating solvation in the modeling system. Wang *et al.* proposed a hybrid model (containing explicit water layer and implicit solvation) to simulate NITRR at the water/Cu interface[105]. By introducing fractional charges, the pH values on the water/Cu interface can be implicitly controlled. By benchmarking with the potential of zero charges (PZC) of Cu, this model is sufficiently accurate to apply in other metal catalytic systems as a computational model that can control pH values at the water/metal interfaces. In a recent study, Tu *et al.* constructed a model containing triple-layer $TiO_2(101)$ with a 3×3 supercell, an alkali cation, and a water molecule to keep ion concentration[106]. According to the simulation results, the N- and C-intermediates can be stabilized around

alkali cations by the short-range electrostatic interaction. Therefore, the roles of alkali cations beyond surface charge balancing also need special attention in future simulations. With the rational construction of SAC-based NITRR model systems, the simulation results will be closer to the experimental results, thus enabling effective guidance for catalyst design and synthesis.

DECLARATIONS

Authors' contributions

Proposed the topic of this review: Li Z
Performed literature survey and prepared the manuscript: Li Z, Yang C, Yao L
Collectively discussed and revised the manuscript: Li Z, Xu B, Zhu W
Review, conceptualization, and supervision: Zhu W, Cui Y

Availability of data and materials

Not applicable.

Financial support and sponsorship

This work was supported by the National Natural Science Foundation of China (22176086), National Key R&D Program of China (2022YFC3204004), Natural Science Foundation of Jiangsu Province (BK20210189), State Key Laboratory of Pollution Control and Resource Reuse, the Fundamental Research Funds for the Central Universities (021114380183, 021114380189, 021114380199), the Research Funds from Frontiers Science Center for Critical Earth Material Cycling of Nanjing University, Research Funds for Jiangsu Distinguished Professor, and Carbon Peaking and Carbon Neutrality Technological Innovation Foundation of Jiangsu Province (BE2022861), the Special Basic Research Service for the Central Level Public Welfare Research Institute (GYZX240503), and the Foundation of Key Laboratory of Pulp and Paper Science & Technology of Ministry of Education (No. KF 202206), Qilu University of Technology.

Conflicts of interest

All authors declared that there are no conflicts of interest.

Ethical approval and consent to participate

Not applicable.

Consent for publication

Not applicable.

Copyright

© The Author(s) 2024.

REFERENCES

1. Suryanto BHR, Matuszek K, Choi J, et al. Nitrogen reduction to ammonia at high efficiency and rates based on a phosphonium proton shuttle. *Science* 2021;372:1187-91. DOI
2. Wang S, Ichihara F, Pang H, Chen H, Ye J. Nitrogen fixation reaction derived from nanostructured catalytic materials. *Adv Funct Mater* 2018;28:1803309. DOI
3. Chen Z, Dolfing J, Zhuang S, Wu Y. Periphytic biofilms-mediated microbial interactions and their impact on the nitrogen cycle in rice paddies. *Eco Environ Health* 2022;1:172-80. DOI PubMed PMC
4. Wang Y, Zhou W, Jia R, Yu Y, Zhang B. Unveiling the activity origin of a copper-based electrocatalyst for selective nitrate reduction to ammonia. *Angew Chem Int Ed* 2020;59:5350-4. DOI
5. Rosca V, Duca M, de Groot MT, Koper MT. Nitrogen cycle electrocatalysis. *Chem Rev* 2009;109:2209-44. DOI PubMed
6. Penuelas J, Sardans J. Human-driven global nutrient imbalances increase risks to health. *Eco Environ Health* 2023;2:246-51. DOI PubMed PMC

7. Duca M, Koper MTM. Powering denitrification: the perspectives of electrocatalytic nitrate reduction. *Energy Environ Sci* 2012;5:9726-42. DOI
8. Du R, Cao S, Peng Y, Zhang H, Wang S. Combined partial denitrification (PD)-Anammox: A method for high nitrate wastewater treatment. *Environ Int* 2019;126:707-16. DOI
9. Shen J, He R, Han W, Sun X, Li J, Wang L. Biological denitrification of high-nitrate wastewater in a modified anoxic/oxic-membrane bioreactor (A/O-MBR). *J Hazard Mater* 2009;172:595-600. DOI
10. Zheng W, Zhu L, Yan Z, et al. Self-Activated Ni Cathode for Electrocatalytic Nitrate Reduction to Ammonia: From Fundamentals to Scale-Up for Treatment of Industrial Wastewater. *Environ Sci Technol* 2021;55:13231-43. DOI
11. Zhang C, Zhang Y, Deng R, et al. Enabling logistics automation in nanofactory: cobalt phosphide embedded metal-organic frameworks for efficient electrocatalytic nitrate reduction to ammonia. *Adv Mater* 2024:e2313844. DOI
12. Li J, Zhan G, Yang J, et al. Efficient ammonia electrosynthesis from nitrate on strained ruthenium nanoclusters. *J Am Chem Soc* 2020;142:7036-46. DOI
13. Jia R, Wang Y, Wang C, Ling Y, Yu Y, Zhang B. Boosting selective nitrate electroreduction to ammonium by constructing oxygen vacancies in TiO_2. *ACS Catal* 2020;10:3533-40. DOI
14. Gao Z, Lai Y, Tao Y, Xiao L, Zhang L, Luo F. Constructing well-defined and robust Th-MOF-supported single-site copper for production and storage of ammonia from electroreduction of nitrate. *ACS Cent Sci* 2021;7:1066-72. DOI PubMed PMC
15. Chen G, Yuan Y, Jiang H, et al. Electrochemical reduction of nitrate to ammonia via direct eight-electron transfer using a copper-molecular solid catalyst. *Nat Energy* 2020;5:605-13. DOI
16. Sun WJ, Ji HQ, Li LX, et al. Built-in electric field triggered interfacial accumulation effect for efficient nitrate removal at ultra-low concentration and electroreduction to ammonia. *Angew Chem Int Ed* 2021;60:22933-9. DOI
17. Carvalho OQ, Marks R, Nguyen HKK, et al. Role of electronic structure on nitrate reduction to ammonium: a periodic journey. *J Am Chem Soc* 2022;144:14809-18. DOI
18. Fan X, Liang J, Zhang L, et al. Enhanced electrocatalytic nitrate reduction to ammonia using plasma-induced oxygen vacancies in $CoTiO_{3-x}$ nanofiber. *Carbon Neutral* 2022;1:6-13. DOI
19. Chen Y, Ji S, Chen C, Peng Q, Wang D, Li Y. Single-atom catalysts: synthetic strategies and electrochemical applications. *Joule* 2018;2:1242-64. DOI
20. Ding S, Yin L, Lyu Z, et al. Wearable microgrids empowered by single-atom materials. *Innova Mater* 2023;2:100023. DOI
21. Chakraborty R, K V, Pradhan M, Nayak AK. Recent advancement of biomass-derived porous carbon based materials for energy and environmental remediation applications. *J Mater Chem A* 2022;10:6965-7005. DOI
22. Wang Y, Su H, He Y, et al. Advanced electrocatalysts with single-metal-atom active sites. *Chem Rev* 2020;120:12217-314. DOI
23. Zhao J, Xue S, Barber J, Zhou Y, Meng J, Ke X. An overview of Cu-based heterogeneous electrocatalysts for CO_2 reduction. *J Mater Chem A* 2020;8:4700-34. DOI
24. Wei Y, Xia H, Yan W, Zhang J. Recent processing of interaction mechanisms of single metallic atom/clusters in energy electrocatalysis. *Energy Mater* 2023;3:300033. DOI
25. Gong X, Song P, Han C, Xiao Y, Mei X, Xu W. Heterogeneous single-atom catalysts for energy process: recent progress, applications and challenges. *Energy Mater* 2023;3:300016. DOI
26. Cheng XF, He JH, Ji HQ, et al. Coordination symmetry breaking of single-atom catalysts for robust and efficient nitrate electroreduction to ammonia. *Adv Mater* 2022;34:e2205767. DOI
27. Zhu C, Shi Q, Feng S, Du D, Lin Y. Single-atom catalysts for electrochemical water splitting. *ACS Energy Lett* 2018;3:1713-21. DOI
28. Shang W, Liu W, Cai X, et al. Insights into atomically dispersed reactive centers on g-C_3N_4 photocatalysts for water splitting. *Adv Powder Mater* 2023;2:100094. DOI
29. Jiang F, Li Y, Pan Y. Design principles of single-atom catalysts for oxygen evolution reaction: from targeted structures to active sites. *Adv Mater* 2024;36:e2306309. DOI
30. Zhang J, Tang X, Hong Y, et al. Carbon-based single-atom catalysts in advanced oxidation reactions for water remediation: from materials to reaction pathways. *Eco Environ Health* 2023;2:47-60. DOI PubMed PMC
31. Wan C, Duan X, Huang Y. Molecular design of single-atom catalysts for oxygen reduction reaction. *Adv Energy Mater* 2020;10:1903815. DOI
32. Li Z, Ma R, Ju Q, et al. Spin engineering of single-site metal catalysts. *Innovation* 2022;3:100268. DOI PubMed PMC
33. Han J, Bian J, Sun C. Recent advances in single-atom electrocatalysts for oxygen reduction reaction. *Research* 2020;2020:9512763. DOI PubMed PMC
34. Lu B, Liu Q, Nichols F, et al. Oxygen reduction reaction catalyzed by carbon-supported platinum few-atom clusters: significant enhancement by doping of atomic cobalt. *Research* 2020;2020:9167829. DOI PubMed PMC
35. Shao Y, Yuan Q, Zhou J. Single-atom catalysts and dual-atom catalysts for CO_2 electroreduction: competition or cooperation? *Small* 2023;19:e2303446. DOI
36. Tang T, Wang Z, Guan J. Achievements and challenges of copper-based single-atom catalysts for the reduction of carbon dioxide to C2+ products. *Exploration* 2023;3:20230011. DOI PubMed PMC
37. Li M, Wang H, Luo W, Sherrell PC, Chen J, Yang J. Heterogeneous single-atom catalysts for electrochemical CO_2 reduction reaction. *Adv Mater* 2020;32:e2001848. DOI
38. Li X, Chen Y, Zhan X, et al. Strategies for enhancing electrochemical CO_2 reduction to multi-carbon fuels on copper. *Innov Mater*

2023;1:100014. DOI

39. Li J, Chen S, Quan F, et al. Accelerated dinitrogen electroreduction to ammonia via interfacial polarization triggered by single-atom protrusions. *Chem* 2020;6:885-901. DOI
40. Wei X, Liu Y, Zhu X, et al. Dynamic reconstitution between copper single atoms and clusters for electrocatalytic urea synthesis. *Adv Mater* 2023;35:e2300020. DOI
41. Chen H, Zhang C, Sheng L, et al. Copper single-atom catalyst as a high-performance electrocatalyst for nitrate-ammonium conversion. *J Hazard Mater* 2022;434:128892. DOI
42. Wang L, Wang D, Li Y. Single-atom catalysis for carbon neutrality. *Carbon Energy* 2022;4:1021-79. DOI
43. Wang Z, Liu S, Wang M, et al. In situ construction of metal-organic frameworks as smart channels for the effective electrocatalytic reduction of nitrate at ultralow concentrations to ammonia. *ACS Catal* 2023;13:9125-35. DOI
44. Hu T, Wang C, Wang M, Li CM, Guo C. Theoretical insights into superior nitrate reduction to ammonia performance of copper catalysts. *ACS Catal* 2021;11:14417-27. DOI
45. Zhao X, Jia X, He Y, et al. Two-dimensional BCN matrix inlaid with single-atom-Cu driven electrochemical nitrate reduction reaction to achieve sustainable industrial-grade production of ammonia. *Appl Mater Today* 2021;25:101206. DOI
46. Zhao X, Li X, Zhang H, et al. Atomic-dispersed copper simultaneously achieve high-efficiency removal and high-value-added conversion to ammonia of nitrate in sewage. *J Hazard Mater* 2022;424:127319. DOI
47. Zhu T, Chen Q, Liao P, et al. Single-atom Cu catalysts for enhanced electrocatalytic nitrate reduction with significant alleviation of nitrite production. *Small* 2020;16:e2004526. DOI
48. Zhao X, Geng Q, Dong F, et al. Boosting the selectivity and efficiency of nitrate reduction to ammonia with a single-atom Cu electrocatalyst. *Chem Eng J* 2023;466:143314. DOI
49. Xue Y, Yu Q, Ma Q, et al. Electrocatalytic hydrogenation boosts reduction of nitrate to ammonia over single-atom Cu with Cu(I)-N_3 C_1 sites. *Environ Sci Technol* 2022;56:14797-807. DOI
50. Wang Y, Zhang W, Wen W, et al. Atomically dispersed unsaturated Cu-N_3 sites on high-curvature hierarchically porous carbon nanotube for synergetic enhanced nitrate electroreduction to ammonia. *Adv Funct Mater* 2023;33:2302651. DOI
51. Wang H, Yao Y, Zhan J, et al. P-modified single-atom Cu catalyst boosting electrocatalytic performance of NO_3^- reduction to NH_3. *ChemCatChem* 2023;15:e202201633. DOI
52. Li P, Liao L, Fang Z, Su G, Jin Z, Yu G. A multifunctional copper single-atom electrocatalyst aerogel for smart sensing and producing ammonia from nitrate. *Proc Natl Acad Sci USA* 2023;120:e2305489120. DOI PubMed PMC
53. Yang J, Qi H, Li A, et al. Potential-driven restructuring of Cu single atoms to nanoparticles for boosting the electrochemical reduction of nitrate to ammonia. *J Am Chem Soc* 2022;144:12062-71. DOI
54. Nielsen SE. Ammonia synthesis: catalyst and technologies. In: Flank WH, Abraham MA, Matthews MA, editors. Innovations in industrial and engineering chemistry. Washington: American Chemical Society; 2008. pp. 15-39. DOI
55. Yoshino H, Kawase Y. Kinetic modeling and simulation of zero-valent iron wastewater treatment process: simultaneous reduction of nitrate, hydrogen peroxide, and phosphate in semiconductor acidic wastewater. *Ind Eng Chem Res* 2013;52:17829-40. DOI
56. Wu ZY, Karamad M, Yong X, et al. Electrochemical ammonia synthesis via nitrate reduction on Fe single atom catalyst. *Nat Commun* 2021;12:2870. DOI PubMed PMC
57. Song Q, Li M, Hou X, et al. Anchored Fe atoms for N=O bond activation to boost electrocatalytic nitrate reduction at low concentrations. *Appl Catal B Environ* 2022;317:121721. DOI
58. Zhang W, Dong H, Zhou L, et al. Fe single-atom catalysts with pre-organized coordination structure for efficient electrochemical nitrate reduction to ammonia. *Appl Catal B Environ* 2022;317:121750. DOI
59. Xu J, Zhang S, Liu H, et al. Breaking local charge symmetry of iron single atoms for efficient electrocatalytic nitrate reduction to ammonia. *Angew Chem Int Ed* 2023;62:e202308044. DOI
60. Liu F, Li J, An N, Huang J, Liu X, Li M. Highly active electroreduction of nitrates to ammonia over a zeolitic imidazolium framework-derived Fe single-atom catalyst with sulfur-modified asymmetric active centers. *J Hazard Mater* 2024;465:133484. DOI
61. Wang Z, Liu S, Zhao X, et al. Interfacial defect engineering triggered by single atom doping for highly efficient electrocatalytic nitrate reduction to ammonia. *ACS Mater Lett* 2023;5:1018-26. DOI
62. Zhao J, Ren X, Liu X, et al. Zn single atom on N-doped carbon: highly active and selective catalyst for electrochemical reduction of nitrate to ammonia. *Chem Eng J* 2023;452:139533. DOI
63. Yang L, Wang C, Li Y, et al. Frustrated lewis pairs on Zr single atoms supported N-doped TiO_{2-x} catalysts for electrochemical nitrate reduction to ammonia. *Adv Funct Mater* 2024:2401094. DOI
64. Ajmal S, Kumar A, Mushtaq MA, et al. Uniting synergistic effect of single-Ni site and electric field of B- bridged-N for boosted electrocatalytic nitrate reduction to ammonia. *Small* 2024:e2310082. DOI
65. Li J, Li M, An N, et al. Boosted ammonium production by single cobalt atom catalysts with high Faradic efficiencies. *Proc Natl Acad Sci USA* 2022;119:e2123450119. DOI PubMed PMC
66. Wang C, Markovic NM, Stamenkovic VR. Advanced platinum alloy electrocatalysts for the oxygen reduction reaction. *ACS Catal* 2012;2:891-8. DOI
67. Li S, Dong M, Peng M, et al. Crystal-phase engineering of PdCu nanoalloys facilitates selective hydrodeoxygenation at room temperature. *Innovation* 2022;3:100189. DOI PubMed PMC
68. Zhang L, Dang Y, Zhou X, et al. Direct conversion of CO_2 to a jet fuel over CoFe alloy catalysts. *Innovation* 2021;2:100170. DOI

PubMed PMC

69. Vandevyvere T, Sabbe MK, Mendes PS, Thybaut JW, Lauwaert J. NiCu-based catalysts for the low-temperature hydrodeoxygenation of anisole: Effect of the metal ratio on SiO_2 and γ-Al_2O_3 supports. *Green Carbon* 2023;1:170-84. DOI
70. Wang Y, Xu A, Wang Z, et al. Enhanced nitrate-to-ammonia activity on copper-nickel alloys via tuning of intermediate adsorption. *J Am Chem Soc* 2020;142:5702-8. DOI
71. Du C, Lu S, Wang J, et al. Selectively reducing nitrate into NH_3 in neutral media by PdCu single-atom alloy electrocatalysis. *ACS Catal* 2023;13:10560-9. DOI
72. Liu H, Lang X, Zhu C, et al. Efficient electrochemical nitrate reduction to ammonia with copper-supported rhodium cluster and single-atom catalysts. *Angew Chem Int Ed* 2022;61:e202202556. DOI
73. Cai J, Wei Y, Cao A, et al. Electrocatalytic nitrate-to-ammonia conversion with ~100% faradaic efficiency via single-atom alloying. *Appl Catal B Environ* 2022;316:121683. DOI
74. Yin H, Peng Y, Li J. Electrocatalytic reduction of nitrate to ammonia via a Au/Cu single atom alloy catalyst. *Environ Sci Technol* 2023;57:3134-44. DOI
75. Zhang Y, Chen X, Wang W, Yin L, Crittenden JC. Electrocatalytic nitrate reduction to ammonia on defective Au1Cu (111) single-atom alloys. *Appl Catal B Environ* 2022;310:121346. DOI
76. Chen K, Ma Z, Li X, Kang J, Ma D, Chu K. Single-atom Bi alloyed Pd metallene for nitrate electroreduction to ammonia. *Adv Funct Mater* 2023;33:2209890. DOI
77. Xie M, Tang S, Li Z, et al. Intermetallic single-atom alloy In-Pd bimetallene for neutral electrosynthesis of ammonia from nitrate. *J Am Chem Soc* 2023;145:13957-67. DOI
78. Wu X, Nazemi M, Gupta S, et al. Contrasting capability of single atom palladium for thermocatalytic versus electrocatalytic nitrate reduction reaction. *ACS Catal* 2023;13:6804-12. DOI
79. Ji S, Chen Y, Wang X, Zhang Z, Wang D, Li Y. Chemical synthesis of single atomic site catalysts. *Chem Rev* 2020;120:11900-55. DOI
80. Fei H, Dong J, Wan C, et al. Microwave-assisted rapid synthesis of graphene-supported single atomic metals. *Adv Mater* 2018;30:e1802146. DOI
81. Zhang L, Banis MN, Sun X. Single-atom catalysts by the atomic layer deposition technique. *Natl Sci Rev* 2018;5:628-30. DOI
82. Qiu HJ, Ito Y, Cong W, et al. Nanoporous graphene with single-atom nickel dopants: an efficient and stable catalyst for electrochemical hydrogen production. *Angew Chem Int Ed* 2015;54:14031-5. DOI
83. Ali H, Masar M, Guler AC, Urbanek M, Machovsky M, Kuritka I. Heterojunction-based photocatalytic nitrogen fixation: principles and current progress. *Nanoscale Adv* 2021;3:6358-72. DOI PubMed PMC
84. Zhao Y, Shi R, Bian X, et al. Ammonia detection methods in photocatalytic and electrocatalytic experiments: how to improve the reliability of NH_3 production rates? *Adv Sci* 2019;6:1802109. DOI PubMed PMC
85. Hodgetts RY, Kiryutin AS, Nichols P, et al. Refining universal procedures for ammonium quantification via rapid ^{1}H NMR analysis for dinitrogen reduction studies. *ACS Energy Lett* 2020;5:736-41. DOI
86. Li Z, Wang L, Cai Y, Zhang J, Zhu W. Electrochemically reconstructed copper-polypyrrole nanofiber network for remediating nitrate-containing water at neutral pH. *J Hazard Mater* 2022;440:129828. DOI
87. Wendimu G, Hussen A, Mohan BR. Wax screen-based fabrication of paper devices for the determination of iron in particulates of selected welding fumes in Addis Ababa, Ethiopia. *Bull Chem Soc Eth* 2024;38:563-76. DOI
88. Sarma BB, Maurer F, Doronkin DE, Grunwaldt JD. Design of single-atom catalysts and tracking their fate using operando and advanced X-ray spectroscopic tools. *Chem Rev* 2023;123:379-444. DOI PubMed PMC
89. Wang X, Wu X, Ma W, et al. Free-standing membrane incorporating single-atom catalysts for ultrafast electroreduction of low-concentration nitrate. *Proc Natl Acad Sci USA* 2023;120:e2217703120. DOI PubMed PMC
90. Liu X, Chen S, Wang H, et al. Lattice confined Ru single sites in hollow Co_9S_8 polyhedron triggering Co-S-Ru catalytic centers for rechargeable Zn-air battery. *Nano Res* 2023;16:6701-9. DOI
91. Sun H, Sun L, Liao Y, et al. Atomically imaging single atom catalysts and their behaviors by scanning tunneling microscopy. *EES Catal* 2023;1:794-809. DOI
92. Zhang L, Li Y, Zhang L, et al. Direct visualization of the evolution of a single-atomic cobalt catalyst from melting nanoparticles with carbon dissolution. *Adv Sci* 2022;9:e2200592. DOI PubMed PMC
93. Li X, Yang X, Zhang J, Huang Y, Liu B. In situ/operando techniques for characterization of single-atom catalysts. *ACS Catal* 2019;9:2521-31. DOI
94. Zhang N, Zhang G, Shen P, Zhang H, Ma D, Chu K. Lewis acid Fe-V pairs promote nitrate electroreduction to ammonia. *Adv Funct Mater* 2023;33:2211537. DOI
95. Song W, Yue L, Fan X, et al. Recent progress and strategies on the design of catalysts for electrochemical ammonia synthesis from nitrate reduction. *Inorg Chem Front* 2023;10:3489-514. DOI
96. Xiang T, Liang Y, Zeng Y, et al. Transition metal single-atom catalysts for the electrocatalytic nitrate reduction: mechanism, synthesis, characterization, application, and prospects. *Small* 2023;19:e2303732. DOI
97. Wang S, Li L, Hui KS, et al. Non-noble single-atom alloy for electrocatalytic nitrate reduction using hierarchical high-throughput screening. *Nano Energy* 2023;113:108543. DOI
98. Niu H, Zhang Z, Wang X, Wan X, Shao C, Guo Y. Theoretical insights into the mechanism of selective nitrate-to-ammonia

electroreduction on single-atom catalysts. *Adv Funct Mater* 2021;31:2008533. DOI

99. Zhu S, Qin M, Chen L, et al. Theoretical investigation of electrocatalytic reduction of nitrates to ammonia on highly efficient and selective g-C_2N monolayer-supported single transition-metal atoms. *J Phys Chem Lett* 2023;14:4185-91. DOI
100. Lai J, Zhang Z, Yang X, et al. Opening the black box: Insights into the restructuring mechanism to steer catalytic performance. *Innov Mater* 2023;1:100020. DOI
101. Bai X, Zhao X, Zhang Y, et al. Dynamic stability of copper single-atom catalysts under working conditions. *J Am Chem Soc* 2022;144:17140-8. DOI
102. Zhang H, Liu G, Shi L, Ye J. Single-atom catalysts: emerging multifunctional materials in heterogeneous catalysis. *Adv Energy Mater* 2018;8:1701343. DOI
103. Liberto G, Pacchioni G. Modeling single-atom catalysis. *Adv Mater* 2023;35:e2307150. DOI PubMed
104. Burke K, Wagner LO. DFT in a nutshell. *Int J of Quantum Chem* 2013;113:96-101. DOI
105. Wang Y, Qin X, Shao M. First-principles mechanistic study on nitrate reduction reactions on copper surfaces: effects of crystal facets and pH. *J Catal* 2021;400:62-70. DOI
106. Tu X, Zhu X, Bo S, et al. A universal approach for sustainable urea synthesis via intermediate assembly at the electrode/electrolyte interface. *Angew Chem Int Ed* 2024;63:e202317087. DOI